Rayleigh-Bénard Convection in a Hele-Shaw Cell

A Numerical Study

C. Günther, U. Müller
Institut für Reaktorbauelemente

Kernforschungszentrum Karlsruhe

KERNFORSCHUNGSZENTRUM KARLSRUHE

Institut für Reaktorbauelemente

KfK 4212

Rayleigh-Bénard Convection in a Hele-Shaw Cell - A Numerical Study

C. Günther, U. Müller

Contents

Zusammenfassung

Rayleigh-Bénard-Konvektion in einer Hele-Shaw-Zelle
Eine numerische Untersuchung

Freie Konvektion in engen senkrechten Spalten, welche von unten beheizt und oben gekühlt werden, zeigt im überkritischen Bereich mehrere verschiedene Strömungs-formen, wie in Experimenten gezeigt werden konnte. Die vorliegende Untersuchung hat das Ziel, die in einer schmalen Hele-Shaw-Zelle beobachteten Strömungen numerisch nachzuvollziehen.

Die wesentliche zugrundeliegende Annahme besteht darin, daß die Strömung in bestimmter Näherung als zweidimensional vorausgesetzt werden kann. Diese Annahme ist äquivalent zu dem Ansatz, der darin besteht, in der Richtung senkrecht zum Spalt eine Galerkin-Approximation mit ein oder zwei Funktionen zu verwenden und die verbleibenden zweidimensionalen Gleichungen mit einem Differenzenverfahren zu lösen.

Die Rechnungen ergeben realistische Werte für die kritischen Rayleighzahlen für Einsetzen stationärer und oszillatorischer Konvektion. Die meisten im Experiment gefundenen Strömungen können auch numerisch simuliert werden. In einem Falle kann gezeigt werden, daß zu einer bestimmten Rayleighzahl fünf verschiedene stabile Strömungen auftreten. Die verschiedenen stabilen Strömungszustände sind durch eine Vielzahl komplexer Verzweigungen verbunden. Zusätzlich wird gezeigt, daß eine realistische Beschreibung der beobachteten Strömungen nicht erreicht wird, wenn nur das Darcy-Gesetz für Strömung in porösen Medien verwendet wird.

Summary
<u>   </u>

Rayleigh-Bénard Convection in a Hele-Shaw Cell - A Numerical Study

Free convection in narrow vertical gaps heated from below gives rise to
several different flow patterns as has been demonstrated by previous experi-
mental investigations. A numerical study is presented aimed at simulating
the observed flow phenomena in Hele-Shaw cells of small lateral extend.

The numerical study is based on the assumption that the flow is essentially
two-dimensional. This allows an approach using a one-term Galerkin approxima-
tion with respect to the direction perpendicular to the gap and a finite
difference scheme with regard to the coordinates in the plane of the gap. The
calculations result in realistic values for the critical Rayleigh numbers for
the onset of steady and oscillatory convection. Most of the observed unsteady
flow patterns can be simulated numerically. It is shown that five different
stable flow patterns can occur at one particular Rayleigh number. The diffe-
rent stable flow patterns are coupled by a variety of complex transitions.
Moreover the calculations show that a realistic description of the observed
flow phenomena can not be obtained by a simplified model using the Darcy law
in the momentum equation and implying slip flow at the small confining boun-
daries.

1 Introduction

Rayleigh-Bénard convection in small boxes heated from below has received considerable attention in the past decade as a most suitable arrangement for studying the nonlinear behavior of fluid dynamic systems with limited degrees of freedom. Several groups such as those around Ahlers & Behringer (1978, 1982), Bergé (1980), Gollub (1980), and Libchaber (1982, 1983) have carried out extensive experimental and analytical work aimed at clarifying the evolution from steady state to turbulent convection. From a mathematical point of view the transition to turbulent convection may be explained by a finite or infinite sequence of temporal and spatial bifurcations of permanent solutions of the Boussinesq equations. The permanent solutions may be steady, time periodic, quasi-periodic or even strongly aperiodic.

Originally the transition to turbulence was thought of as the uniform disappearance of the coherence time and length scale in the flow. The experiments using small aspect ratio boxes, however, show that the coherence time scale may decrease ahead of the coherence length scale. This may be reasoned by the facts that the low aspect ratio box limits the spatial evolution to only a few discrete modes while allowing many temporal transitions. In the past few years several sequences of temporal transitions have been identified which lead to strong aperiodic time behavior of the state variables. Such states are usually referred to as chaotic (for a review see Eckmann (1981) or Gollub and Benson (1980)).

Although a huge amount of experimental data concerning the various routes to chaotic states is now available, realistic descriptions of these phenomena by analytical or numerical methods are limited.

Three-dimensional numerical experiments have been carried out in the past by McLaughlin and Orszag (1982), Curry et al. (1984), Schubert and Strauss (1982), Kimura and Schubert (1986), Kessler (1984), Grötzbach (1982) and Lipps (1976). Although the computational effort in these works is immense, the parametrization of the problem with respect to spatial and temporal variables remains incomplete.

When calculating three-dimensional complex flows even in small containers, general difficulties exist in obtaining the proper spatial and temporal resolutions.

One way out of this shortcoming is by reducing the spatial degree of freedom of the convective flow even more and considering two-dimensional flow in narrow gaps. In gap flow a reasonable spatial resolution perpendicular to the gap can be achieved with very few Galerkin test functions. For very narrow gaps one test function satisfying the boundary conditions generally proves to be sufficient.

This idea was first suggested by Putin and Tkacheva (1979) and more recently by Koster and Müller (1982, 1984). These authors performed free convection experiments in so-called Hele-Shaw geometries. They observe similar temporal phenomena as those described by Gollub et Benson (1980), Berge and his group and Libchaber et al. (1982). Moreover Koster and Müller (1984) relate their measured local temperature histories to the spatial flow patterns indirectly visualized by holographic interferometry.

Two-dimensional convection in Hele-Shaw cells can be described numerically in some detail without consuming inadequate computational time.

In this paper essential features observed by Koster and Müller (1984) in their experiments are simulated by solving numerically a simplified set of hydrodynamic equations for gap flow employing a finite difference scheme. In particular we shall elaborate the relation between the symmetries of various spatial patterns and the local histories of the temperature and the velocities.

We shall consider a container, two of whose spatial dimensions are of the same order of magnitude while its third dimension in horizontal direction is an order of magnitude smaller. This container is called after Hele-Shaw (1898) a Hele-Shaw cell. Our numerical investigations of convective flow will refer to a container for which $h > b \gg d$ holds with h its height, b its width and d its depth (see fig. 1). More precisely we shall concentrate the calculation on the particular test arrangement of Koster & Müller (1984). This cell had the dimensions $h:b:d = 7:2:0.3$. The cavity is formed by a copper or plexiglas frame sandwiched between glass or plexiglas windows. The cavity is filled with silicon oil of Prandtl number 38.5 and heated at the bottom while cooled at the top.

In order to simulate the experimental conditions closely we shall perform calculations for the two limiting conditions, adiabatic sidewalls and per-

fectly conducting sidewalls and for a representative thermal coupling of the large sidewalls. In each of these cases isothermal horizontal walls will be prescribed.
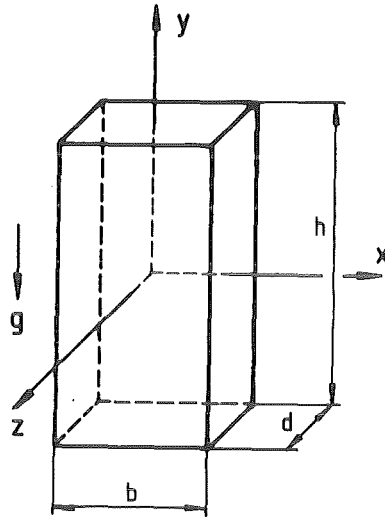

Fig. 1 Principle sketch of a Hele-Shaw cell of small aspect ratio.

2 Related Literature

In convection experiments employing Hele-Shaw cells a set of different steady and oscillatory equilibrium states have been observed. The oscillation may occur in a periodic, quasi-periodic of even stochastic form. For a particular value of the controlling parameter, the Rayleigh number, several different flow patterns can exist, steady state and oscillatory ones. The causes for the transition from steady state to oscillatory flow are still unknown. Many authors treating Rayleigh-Bénard convection in porous media[1] or Hele-Shaw cells e.g. Caltagirone (1975), Horne et al. (1979, 1980) base their explanations on an idea of Howard (1964). Here the onset of oscillations is caused by an instability of the thermal boundary layers in the convection cells. Applying this model to the conditions in a Hele-Shaw cell, the period of oscilla-

---

[1] Since a formal analogy exists between the flow in Hele-Shaw cells and the one in porous media the results of some publications on Rayleigh-Bénard convection in saturated porous bodies can be used for comparison and explanations immediately.

tion τ^* should decrease as Ra^{-2}, Ra being the Rayleigh number, to be defined in (13). Horne et al. and Caltagirone find from numerical calculations $Ra^{-3/2}$. Their calculations are performed for porous media flow based on Darcy's law. They explain the oscillations in the convection cell as circulating thermal waves originating from disturbances in the thermal boundary layer. They refer to this phenomenon as circulating "hot spots". A similar explanation is suggested by Rabinovich (1978).

In recent experimental investigations Lyubimov et al. (1979), Putin & Tkacheva (1979) and Koster and Müller (1982, 1984) study convection in Hele-Shaw cells of different aspect ratios and of different materials of the cell sidewalls. They use water of Prandtl number 6.7 and/or silicon oil of Prandtl number 38.5 as a test fluid and they visualize the flow field and temperature field in the cell (or in the plexiglass walls confining the cell). They find in small aspect ratio boxes that in Hele-Shaw cells several different steady state or oscillatory flow pattern can occur at one particular Rayleigh number and that at highly supercritical Rayleigh numbers stochastic oscillations and random pattern formation occur. These phenomena are succeeded at even higher Rayleigh numbers by a reverse transition to steady state flow.

Frick & Müller (1983) and Günther (1982) both have previously performed numerical computations on laminar convection in Hele-Shaw cells. Frick employes a Galerkin method in his calculations while Günther uses a finite difference method. They have presented numerical results which describe essential features of the observed streamline and isotherm patterns observed by Koster & Müller (1982, 1984). In this paper the previous computations of Günther (1981) will be extended and moreover some open questions will be answered concerning the accuracy of the numerical method employed and the validity of the hydraulic model equations for gap flow.

3   Description of the Mathematical Model and Notation

The convection is described by the Boussinesq equations of the form

$$\frac{\partial}{\partial t} \underset{\sim}{v} + (\underset{\sim}{v} \cdot \nabla)\underset{\sim}{v} = -\frac{1}{\rho_o} \nabla p + \nu \nabla^2 \underset{\sim}{v} + \beta g(T - T_m)\underset{\sim}{e}_y \qquad (1a)$$

$$\frac{\partial}{\partial t} T + (\underset{\sim}{v} \cdot \nabla)T = \varkappa \nabla^2 T \qquad (1b)$$

$$\nabla \cdot \underset{\sim}{v} = 0 \tag{1c}$$

where $\underset{\sim}{v} = (u,v,w)$ is the velocity vector in the Cartesian coordinate system (x,y,z) as displayed in fig. 1, g is the gravitational constant, T is the temperature; $T_m = (T_b+T_t)/2$ is the mean temperature, where T_b and T_t are the temperatures on the bottom and the top of the container, respectively. ν is the kinematic viscosity and $\varkappa$ the thermal diffusivity of the fluid, ρ_o is the average density, p is the reduced pressure, β is the coefficient of thermal expansion, $\underset{\sim}{e_y}$ the unit vector in y-direction and $\nabla = (\frac{\partial}{\partial x}, \frac{\partial}{\partial y}, \frac{\partial}{\partial z})$ is the gradient vector.

For the Hele-Shaw cell placed in a coordinate system according to fig. 1 we have $-b/2 \leq x \leq b/2$; $-h/2 \leq y \leq h/2$, $-d/2 \leq z \leq d/2$ and $d/h \ll 1$. The above equations can be simplified for flow in a narrow gap. We assume that there is no velocity component perpendicular to the large sidewalls, i.e. w = 0. The two other velocity components u, v have a parabolic shape across the gap. Thus we choose the following set for the velocity components:

$$
\begin{aligned}
u(x,y,z,t) &= U(x,y,t) \ f(z) \\
v(x,y,z,t) &= V(x,y,t) \ f(z) \\
w(x,y,z,t) &= 0,
\end{aligned}
\tag{2}
$$

where
$$f = \frac{3}{2} \cdot \left[1 - (2/d)^2 \ z^2\right].$$

The function f(z) is normalized by integration. We set

$$\langle f(z) \rangle \overset{def.}{=} \frac{1}{d} \int_{-\frac{d}{2}}^{\frac{d}{2}} f(z)dz = 1 . \tag{3}$$

Furthermore, we get $\langle f^2 \rangle = 1.2$.

The forms (2) are inserted into the momentum equations (1a) and the resulting expressions are integrated across the gap. We obtain two momentum equations in the x,y plane of the following form:

$$\frac{\partial U}{\partial t} + 1.2 \left[U \frac{\partial U}{\partial x} + V \frac{\partial U}{\partial y} \right] = - \frac{1}{\rho_o} \frac{\partial p}{\partial x} + \nu [\nabla_o^2 U - \frac{1}{K} U] \; , \tag{4a}$$

$$\frac{\partial V}{\partial t} + 1.2 \left[U \frac{\partial V}{\partial x} + V \frac{\partial V}{\partial y} \right] = - \frac{1}{\rho_o} \frac{\partial p}{\partial x} + \nu [\nabla_o^2 V - \frac{1}{K} V] + \beta g \, [<T> - T_m]$$

Here $K = 1/12 \, d^2$ is analogous to the permeability in a saturated porous medium. $\nabla_o = (\frac{\partial}{\partial x}, \frac{\partial}{\partial y})$ is the gradient vector in the gap plane. The continuity equation (1c) reduces now to

$$\frac{\partial U}{\partial x} + \frac{\partial V}{\partial y} = 0 \; . \tag{4b}$$

The equations (4a) contain two frictional terms on the right-hand side. The terms proportional to the velocities model the Poiseuille flow between parallel plates and correspond to the Darcy Law of seepage flow in porous bodies (see Scheidegger 1974). The second contribution to the frictional forces arises from the internal friction in the fluid and the inhibition caused by the small vertical and horizontal sidewalls. This effect is accounted for by the terms $\nabla_o^2 U$ and $\nabla_o^2 V$. They link the present model to the structure of the Navier-Stokes equations. The method of simplifying the Boussinesq equations may be considered as a one term Galerkin procedure with respect to the z coordinate, f(z) being the single trial function satisfying the no-slip condition for the velocities at the large sidewalls. For the flow through porous media Brinkman (1949) derives a similar relationship, which takes into account the drag force of the porous body on the fluid in the form of Darcy's law and the internal friction of the fluid (see Scheidegger, 1972, p. 148).

The occurance of two friction terms in equation (4a) can be explained as follows: The so-called quasi-porous terms $\frac{1}{K} U$ and $\frac{1}{K} V$ describe the influence of the large side-walls on the fluid flow. In the interior regime of the cavity, somewhat away from the small side-walls, these are the dominant terms. If the width b of the cell is larger than the cell height, it justified to take into account only the quasi-porous terms. This approach is not appropriate for small aspect ratios such as h/b = 3.5. We have confirmed this by numerical calculations described later in which we have removed the viscous friction term $\nu \nabla_o^2 \underset{\sim}{U}$ from our model. We have obtained in this case

different numerical results which have little similarity with the available experimental findings.

If the viscous terms $\nabla_o^2 U$ and $\nabla_o^2 V$ are included the no-slip condition $\underset{\sim}{U} = \underset{\sim}{0}$ along the horizontal and small vertical walls of the cavity can be prescribed. The no-slip condition at the small vertical side walls causes a hydrodynamic boundary layer to be formed. The frame of our model if only porous friction is assumed seems to be effective! The size δ of this boundary layer, – in consequence of the aforementioned arguments –, is only determined by the viscous terms and not by the quasi-porous terms in equation (4a).

The energy conservation equation keeps its basic form. However, the temperature T is to be replaced by its integral average value $\hat{T} = \langle T \rangle$ across the gap. The transport term $w \frac{\partial \hat{T}}{\partial z}$ vanishes. The expression for T will generally depend on the thermal boundary conditions at the sidewalls which we discuss next.

First of all we recall that no slip conditions hold on all boundaries confining the cavity, i.e.

$$\underset{\sim}{v} = \underset{\sim}{0} \quad \text{on all rigid boundaries.} \tag{5}$$

As already mentioned, constant temperatures T_b and T_t at the lower and upper horizontal boundaries, respectively, are prescribed in all cases.

On the vertical walls we consider in most of the calculations the two limiting conditions, either the vanishing of the heat flux at the sidewalls or perfectly conducting sidewalls. In the first case, we require

$$\frac{\partial T}{\partial n} = 0 \quad \text{on adiabatic sidewalls} \tag{6}$$

where n denotes the normal direction on the sidewall.

For perfectly conducting large sidewalls the boundary condition has the general form

$$T(x,y,\pm\tfrac{d}{2}, t) = T_m - \frac{y}{h}(T_b - T_t) \equiv T_B(x,y) \tag{7}$$

Similar relations hold also for the perfectly conducting small sidewalls.

The thermal boundary conditions for sidewalls of uniform thickness d_s can be generalized by admitting a finite heat conductivity for the wall material. We assume that the temperature at the outside of the large side walls is $T_B(x,y)$. We model its thermal interaction with the fluid in the cavity by a boundary condition of the third kind, i.e. by the heat flux relation at the wall surface inside the gap

$$\frac{\partial T}{\partial n} = \alpha(T - T_B) \tag{8}$$

with

$$\alpha = \frac{\lambda_s}{\lambda_1} \frac{1}{d_w} \quad ,$$

Here λ_s and λ_1 are the heat conductivities of the wall and the liquid, respectively. The condition (8) is a reasonable approximation for thin side walls only. It must be used with some caution in the case of unsteady flows. Nevertheless, it may serve as a good means for studying the thermal effect of sidewalls with finite heat conductivity. The two cases adiabatic and perfectly conducting side walls can be obtained from eq. (8) by taking the limits for $\alpha \to 0$ and $\alpha \to \infty$. We use eq. (8) and the heat balance equation (1b) now to derive a general equation for the averaged temperature $\hat{T}$. We take into account the symmetry of the temperature distribution across the gap and the boundary conditions at $z = \pm d/2$ and represent the temperature by a power series in z of the form

$$T(x,y,z,t) = T_B(x,y) + T(x,y,t)\, g(z) \tag{9}$$
$$g(z) = a + b \cdot \frac{4}{d^2} z^2 + \dots$$

In our approximation we take into account only quadratic terms in z. The coefficients a and b are determined by employing the boundary condition (8) and by normalizing g(z) such that

$$<g(z)> = 1$$

We get

$$g(z) = \left(1 - \frac{1}{3\left(\frac{4}{\alpha \cdot d} + 1\right)}\right)^{-1} \left[1 - \frac{z^2}{\frac{d}{\alpha} + \frac{d^2}{4}}\right] \tag{10}$$

Introducing the expression (9) together with the relationship (10) into equation (1b) and integrating across the gap we obtain for the mean temperature $\hat{T}$ the differential equation

$$\frac{\partial}{\partial t}\hat{T} + U\frac{\partial \hat{T}}{\partial x} + V\frac{\partial \hat{T}}{\partial y} + \frac{H}{5}\left[U\frac{\partial(\hat{T}-T_B)}{\partial x} + V\frac{\partial(\hat{T}-T_B)}{\partial y}\right] = \qquad (11)$$

$$= \varkappa\left[\nabla_o^2\hat{T} + \nabla_o^2 T_B - \frac{H}{K}(\hat{T}-T_B)\right]$$

where

$$H = \frac{1}{1 + \dfrac{6}{\alpha\cdot d}} \quad .$$

Equation (11) describes both cases, adiabatic and perfectly conducting side-walls by the limits $\alpha \rightarrow 0$ and $\alpha \rightarrow \infty$ or $H \rightarrow 0$ and $H \rightarrow 1$, respectively. For further considerations we assume that a linear temperature distribution is imposed on the outer surface of the side wall i.e. $T_B(x,y)$ is a linear function of y only.

The set of partial differential equations (4a,b) for the velocity components U, V have to be solved together with the differential equation (11) for the temperature function $\hat{T}$. Boundary conditions for the variables U, V, T on the small sidewalls are evident for U,V and can be derived accordingly for T for the various thermal conditions.

For further numerical treatment of the equations it is convenient to introduce dimensionless variables. We introduce the scaling factors: h for the length scale, $h^2/\varkappa$ for the time, $\varkappa/h$ for the velocity and $\rho_o(\frac{\varkappa}{h})^2$ for the pressure. Furthermore we introduce $\frac{\hat{T} - T_m}{T_b - T_i}$ as the dimensionless temperature. Maintaining the original notation for the variables, we arrive at the following set of equations for the dimensionless variables $\underset{\sim}{U} = (U, V)$, $\hat{T}$, respectively, in the fluid

$$\frac{\partial U}{\partial t} + \frac{6}{5}(\underset{\sim}{U}\cdot\nabla_o)\underset{\sim}{U} = -\nabla_o p + Pr[\nabla_o^2\underset{\sim}{U} - \frac{1}{K^*}\underset{\sim}{U}] + Pr\cdot Ra\cdot\hat{T}\cdot\underset{\sim}{e}_y \quad , \qquad (12a)$$

$$\nabla_o\cdot\underset{\sim}{U} = 0 \quad , \qquad (12b)$$

$$\frac{\partial \hat{T}}{\partial t} + U\frac{\partial \hat{T}}{\partial x} + V\frac{\partial \hat{T}}{\partial y} + \frac{H}{5}V\frac{\partial(\hat{T}-T_B)}{\partial y} = \nabla_o^2\hat{T} + \nabla_o^2 T_B - \frac{H}{K^*}(\hat{T}-T_B) \qquad (12c)$$

where the dimensionless groups and the permeability K^* are defined by the relations

$$Ra = \frac{\beta g (T_b - T_t) \, h^3}{\varkappa \cdot \nu}$$ Rayleigh number,

$$Pr = \frac{\nu}{\varkappa}$$ Prandtl number, (13)

$$1/K^* = 12 \, h^2/d^2$$ permeability group,

$$H = \frac{1}{1 + \dfrac{6}{\alpha'}} \quad , \quad \alpha' = \frac{\lambda_s}{\lambda_1} \cdot \frac{d_1}{d_s}$$ thermal property groups.

($\alpha' =$ Biot number)

The boundary conditions for this set of partial differential equations are given the appropriate notation

$$U = V = 0 \qquad \begin{cases} y = \pm\, 1/2, \quad -\, b/2h \leq x \leq b/2h \\[2ex] x = \pm\, b/2h, \quad -\, 1/2 \leq y \leq 1/2 \end{cases}$$

$$\hat{T} = 1/2 \quad y = -1/2 \; , \quad -\, b/2h \leq x \leq b/2h; \tag{14}$$
$$\hat{T} = -1/2 \quad y = +1/2 \; , \quad -\, b/2h \leq x \leq b/2h.$$

$H = 0$ adiabatic large sidewalls,

$T_B = -y, \; H = 1$ perfectly conducting large sidewalls,

$T_B = -y, \; 0 \leq H \leq 1$ conducting large sidewalls.

The thermal boundary condition at the small sidewalls is given for the adiabatic case only since we shall perform the numerical calculations mostly for this case. We have

$$\frac{\partial \hat{T}}{\partial x} = 0 \, , \quad x = \pm\, b/2h, \quad -1/2 \leqslant Y \leqslant 1/2. \tag{15}$$

The model equations (12) together with the boundary conditions (14) and (15) are solved numerically by using a finite difference method. The numerical procedure is described in the appendix.

4 Characteristics of Permanent Solutions

- Adiabatic Sidewalls

The calculated results are obtained for the following set of parameters. Pr = 38.5, h/b = 3.5, h/d = 23.3. All sidewalls are assumed as adiabatic and the two horizontal walls as isothermal. The calculations are performed employing a grid of 9x33 points. If not otherwise stated, the Rayleigh number is changed by small increments $\Delta Ra/Ra_c \leq 10^{-1}$ for successive runs. Special care is taken to identify transitions of the flow pattern.

For further discussions we explain the concept of "mode". We consider two permanent solutions as belonging to the same mode, if their streamline and isotherm patterns are topological similar at corresponding instants of time. This means that the number of vortices and their relative spatial distribution form a topologically similar picture for that mode. As long as this mode is maintained for varying Rayleigh numbers, all the physical properties of the flow depend smoothly on the Rayleigh number. This statement, of course, holds also for the time averaged Nusselt number Nu and the dimensionless period of oscillation τ^*, quantities which we shall display later as a function of the external control parameter, the Rayleigh number.

Using the mode concept in this sense, our calculations show that the transition from the mode of pure heat conduction to a steady mode of convection occurs first at a critical Rayleigh number $Ra_{c1} = 1.0 \times 10^6$. This transition is initially indicated by a slight deviation of the isotherms from the horizontal (see fig. 2). The streamline pattern displays a single roll, circulating hot fluid from the bottom to the top and vice versa.

The pattern is mirror symmetric with respect to the centerlines of the cavity close to the critical Rayleigh number. However, the single roll becomes tilted for increasing supercritical values of Ra in that it loses its mirror symmetry but still maintains its point to point symmetry with respect to the centre of the rectangle. Congruence is achieved by rotating the streamline or isotherm pattern by an angle of π. We shall refer to this feature as inversion symmetry. The direction of the circulation can be clockwise or counter clockwise depending on the set of initial values for the velocity field. We shall term this dual character of the steady solutions as multiplicity of factor 2.
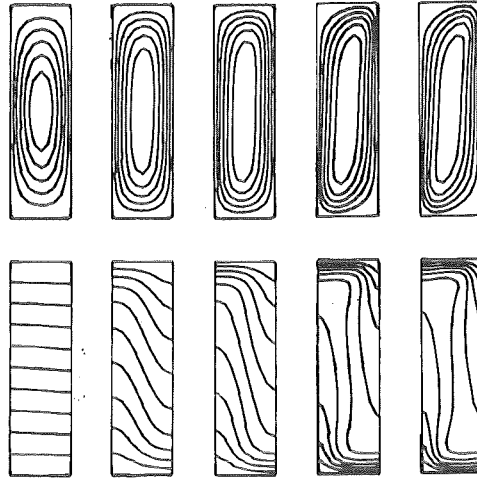
Fig. 2   Steady-state single roll, mode 1, streamline and isotherm pattern
for five different Rayleigh numbers, from Fig. 2a to Fig. 2e read
$Ra \times 10^{-6} = 1, 1.5, 2, 4, 5.$

From the streamline pattern of the strongly tilted single convection roll in
fig. 2e we recognize flow separation at the vertical small sidewalls. Flow
separation occurs in upward flow near the upper corner where the vertical
flow hits the horizontal wall and in downward flow near the corresponding
lower corner of the cavity. More detailed graphs of the streamline patterns
show that small counter-rotating vortices exist in the corners adjacent to
regions of flow separation.

At a second critical Rayleigh number $Ra_{c2} = 5.9 \times 10^6$ the steady single-roll
mode becomes unstable and a new time-periodic solution is established through
a jump transition. This mode is displayed in fig. 3 by a set of instantaneous
streamline and isotherm patterns for a half-period. The streamline patterns
show the decay of a three vortex system to a four vortex system during the
first half period followed by a corresponding reverse process in the second
half period. This oscillatory mode, henceforth termed mode 2, is inversion
symmetric at any instant of time. We refer to this mode as a diagonal oscilla-
tion. Moreover, each instantaneous streamline and isotherm pattern is mirror
symmetric to its counter part occurring during the second half period. We
call this character phase-shift symmetry. The existence of mode 2 up to a
Rayleigh number $Ra = 7 \times 10^6$ has been shown numerically. The range of existence
beyond this value has yet to be explored. We note here that mode 2 has multi-
plicity 1. This means it is impossible to obtain another different flow by

mirror imaging with regard to any symmetry line or to any symmetry point as has been demonstrated for the steady state flow where reflection at the vertical middle line displays the counter-clockwise flow. It is obvious that the occurrence of symmetries reduces the multiplicity of the flow.
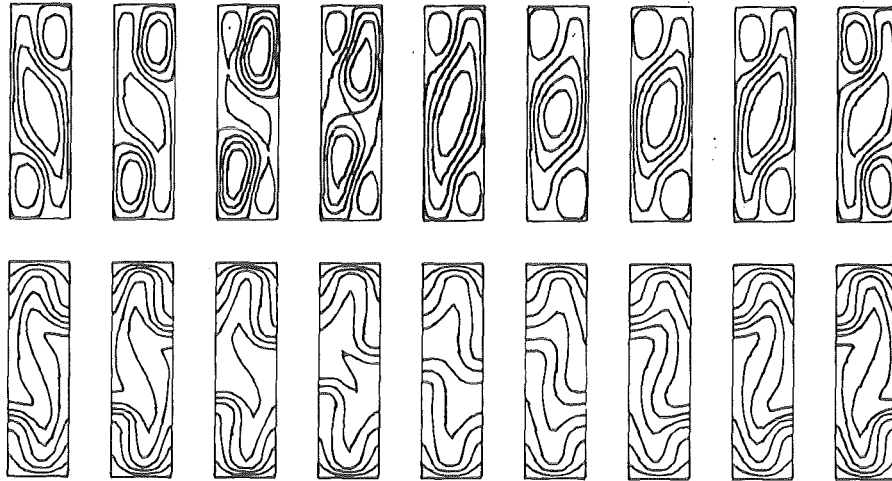

Fig. 3 "Diagonal oscillation" or mode 2; Ra = 6.0×10^6, instantaneous streamline and isotherm patterns for one half-period of oscillation, adiabatic sidewalls.

By decreasing the Rayleigh number by small amounts Δ Ra below the value Ra_{c2} = 5.9×10^6 a hysteresis effect becomes apparent since mode 2 continues to exist down to Ra_{c3} = 5.8×10^6 where another jump transition occurs resulting in another time periodic solution, mode 3. The corresponding set of streamline and isotherm patterns is displayed in fig. 4. The pattern of mode 3 still resembles the pattern of mode 2 as far as the number of instantaneous vortices is concerned. However, the inversion symmetry is lost in mode 3 if compared to mode 2. Once established mode 3 exists even for higher Rayleigh numbers. The existence of mode 3 has been shown numerically up to Ra = 6.1×10^6. Beyond this value a jump transition to mode 4 occurs as will be described below. Mode 3 has multiplicity 2.

If the Rayleigh number is decreased below the value Ra_{c3} = 5.8×10^6, an even more complicated hysteresis effect becomes evident, since the mode 3 continues existence down to a Rayleigh number Ra_{c4} = 5.3×10^6. Here another jump transition occurs to another periodic solution, mode 4. A set of streamline
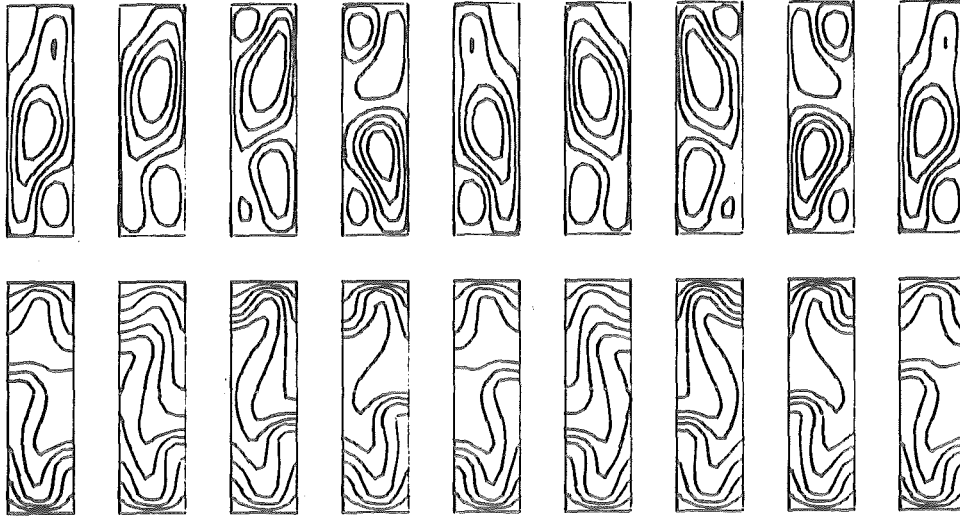
Fig. 4 "Vertical oscillation" or mode 3; Ra = 5.8×10^6, instantaneous streamline and isotherm patterns for one period of oscillation, adiabatic sidewalls.

and isotherm patterns of mode 4 covering about one period of oscillation is shown in fig. 5. The streamline pattern demonstrates that only two and three vortices interact during one period. Moreover, mode 4 exhibits none of the symmetries of mode 2. Mode 4 exists up to a Rayleigh number Ra = 6.6×10^6. Beyond this value a jump transition to mode 2 is observed. Mode 4 contains no spatial symmetries and thus has multiplicity 4.

Decreasing the Rayleigh number below Ra_{c4} = 5.3×10^6 reveals another periodic solution, mode 5, shown in fig. 6. The streamline and isotherm patterns of one period show clearly an interaction of two vortices, one vortex stacked on the top of the other, alternating in growth and shrinkage. For Ra_{c5} = 4×10^6 mode 5 undergoes a jump transition to mode 1. The upper bound of the range of existence of mode 5 is found to be Ra = 6×10^6. Beyond this value a jump transition to mode 4 is realized. Mode 5 has multiplicity 2.

The transition from mode 5 to mode 1 closes the hysteresis loop, connecting the various permanent solutions namely the steady mode 1 and the oscillatory modes 2-5.
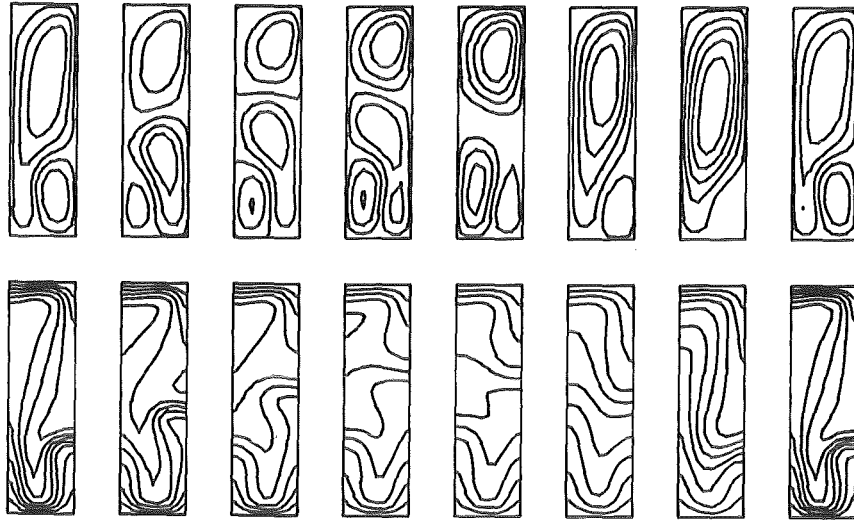
Fig. 5   "Non-symmetric oscillation" or mode 4; Ra = $5.8\text{x}10^6$, instantaneous streamline and isotherm patterns for one period of oscillation, adiabatic sidewalls.
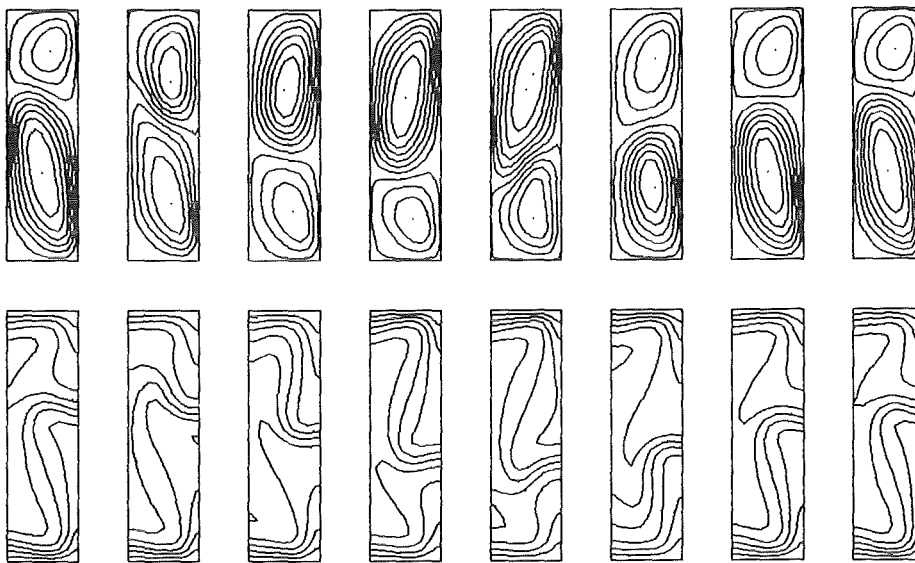

Fig. 6   "Vertical oscillation" or mode 5; Ra = $5.8\text{x}10^6$, instantaneous streamline and isotherm patterns for one period of oscillation, adiabatic sidewalls.

The jump transitions, so far described by pattern identification, can be localized and quantified in a graph of time averaged Nusselt number versus Rayleigh number. This graph is shown in fig. 7. The solid lines are interpolated curves through calculated values of the Nusselt numbers for different modes. Since the Nusselt number is proportional to the integral heat transfer between bottom and top of the cavity, the graph demonstrates clearly that each mode has its own heat transfer characteristic different from that of any other mode. Moreover, there are overlapping ranges of Rayleigh numbers where several modes can exist e.g. all the discussed modes may occur individually in the interval $5.8 \times 10^6 \leq Ra \leq 5.9 \times 10^6$. We recognize from fig. 7, that the steady mode 1 gives the highest heat transfer in the Rayleigh number range discussed while the oscillatory modes result in markedly lower heat transfer rates.
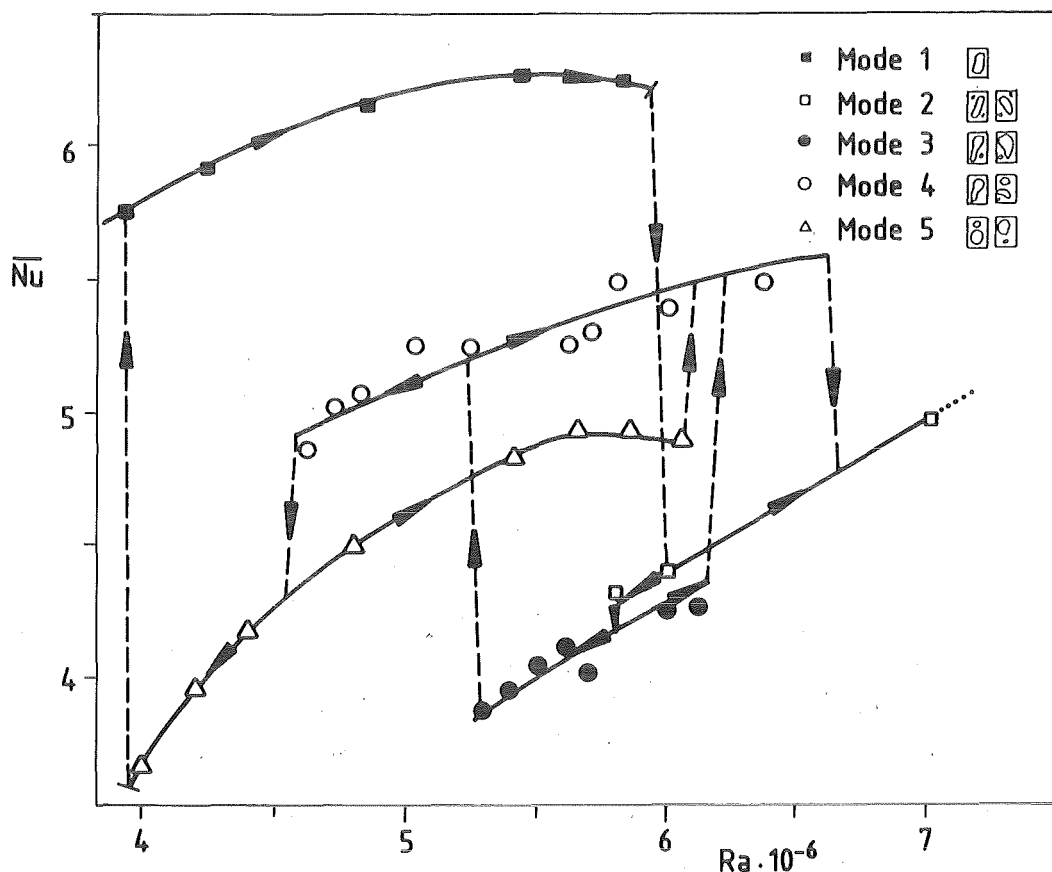

Fig. 7   Time averaged Nusselt number versus Rayleigh number, symbols represent calculated values, solid curves are fitted to the calculated values, dashed curves indicate transitions between the different modes, adiabatic sidewalls.

The single convection roll of mode 1 transports the heat most directly from bottom to top. All the other modes exhibit small recirculation zones in some of the corners for certain time intervals. Since the heat from these recirculation zones has to be transferred to adjacent vortices of larger scale mainly by conduction, the overall heat transfer from bottom to top is smaller than that of mode 1. In this regard mode 4 exhibits the highest heat flux of the periodic solutions, since its streamline and isotherm pattern most resemble those of mode 1.

The periods of oscillation of the time periodic modes 2-5 are shown in fig. 8 as a function of the Rayleigh number. The initial slope of the different curves for onset of oscillation varies between -3 and -5.
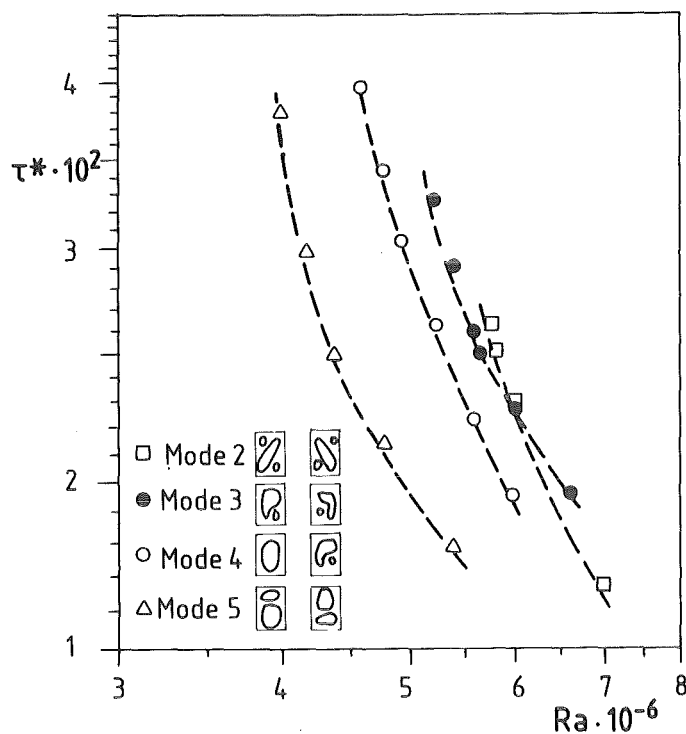

Fig. 8   Dimensionless period of oscillation versus Rayleigh number.

These values differ from the value -2 obtained experimentally by Koster & Müller (1984). The value -2 is consistent with the model of Howard (1964) associated with an instability of the thermal boundary layer initiating the oscillatory flow. The existing discrepancy may be due to an inadequate temporal resolution. Further investigation of this effect is needed.

- Perfectly conducting side walls.

Calculations were also performed for the case that the large side walls of the Hele-Shaw cell are perfectly conducting, the small side walls being adiabatic and the horizontal boundaries isothermal. The following main results were obtained.

The onset of convection occurs at a higher Rayleigh number compared to the previous case of adiabatic sidewalls. We find that $Ra_{c1} = 5.3 \times 10^{7}$. A set of streamline and isotherm patterns for the steady state convection mode 1 is shown in fig. 9. The patterns are symmetric at onset of convection but become tilted to one side for increasing Rayleigh numbers. Stationary recirculating flows develop in two diagonally opposite corners of the cell. The flow pattern possesses inversion symmetry. The tilt of the pattern of the steady solution can be to the right side or the left side of the cell depending on the initial disturbances chosen during the calculation procedure, that is, the mode 1 has multiplicity 2.

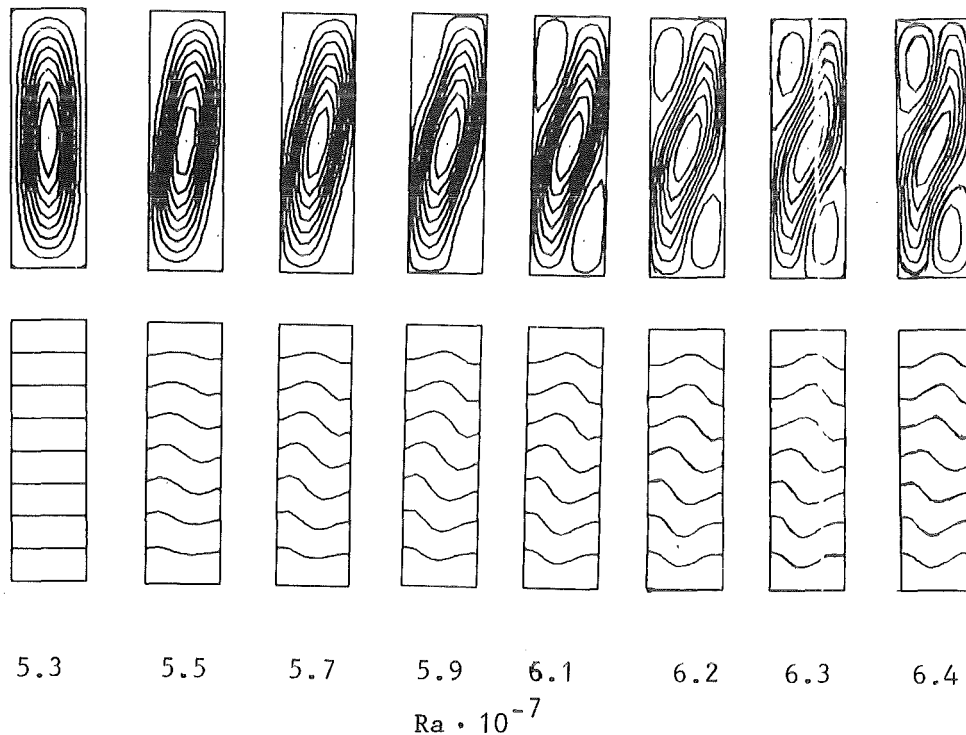| 5.3 | 5.5 | 5.7 | 5.9 | 6.1 | 6.2 | 6.3 | 6.4 |

$$Ra \cdot 10^{-7}$$

Fig. 9   Streamline and isotherm pattern of steady-state convection, mode 1, perfectly conducting large sidewalls, adiabatic small sidewalls.

If the Rayleigh number is raised beyond a second critical value Ra_{c2} = 6.4×10^7, a transition to a time-periodic solution, mode 2, occurs. A set of streamline and isotherm patterns can be seen in fig. 10. The patterns show inversion symmetry at any instant of time since the isotherms are strongly related to the linear temperature profile in the large sidewalls. The deflection of the isotherms from the horizontal is less pronounced than in the case of adiabatic sidewalls.
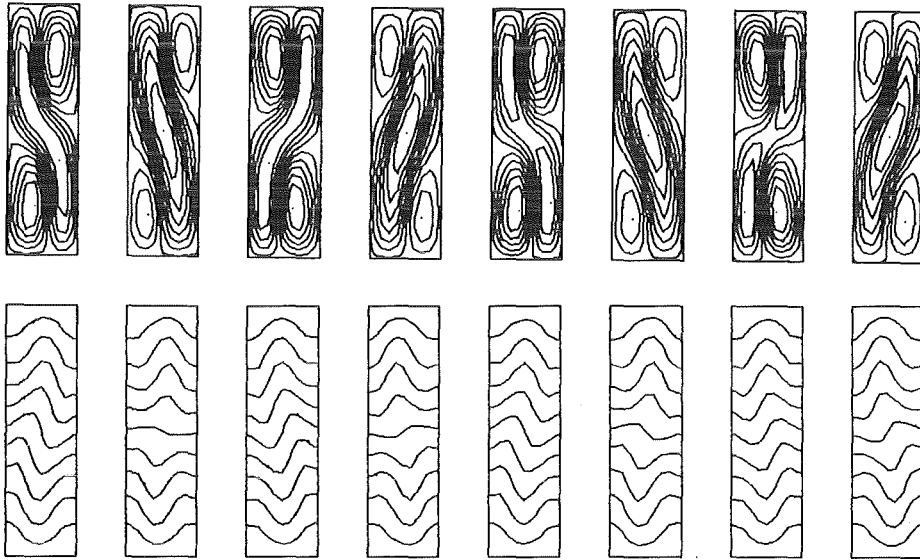

Fig. 10   "Diagonal oscillation"; mode 2; $Ra = 6.5 \times 10^7$, instantaneous stream-
line and isotherm patterns for more than one period of oscillation,
perfectly conducting large sidewalls, adiabatic small sidewalls.

The transition from mode 1 to mode 2 can only be realized numerically if the Rayleigh number is increased instantaneously by very small steps $\Delta Ra \leq 0.05 \times 10^7$; otherwise a jump transition to another steady mode 6 occurs characterized by two slender vortices (see fig. 11).

In the range of Rayleigh numbers $5.3 \times 10^7 \leq Ra \leq 7.0 \times 10^7$ so far investigated the modes 3-5 could not be found. Instead, the previously mentioned steady solution, mode 6, appears beyond $Ra = 6 \times 10^7$ if the increments ΔRa between two permanent states are chosen large enough. In a Rayleigh number range near the second critical, $Ra_{c2} = 6.4 \times 10^7$, mode 6 proves to be quite stable in comparison to mode 2 with regard to jumps in the Rayleigh number. Mode 6 is mirror symmetric with respect to the vertical centerline but is not inversion symmetric.

Mode 6 has multiplicity 2. The latter character is demonstrated by calculations and can be seen in fig. 11b.

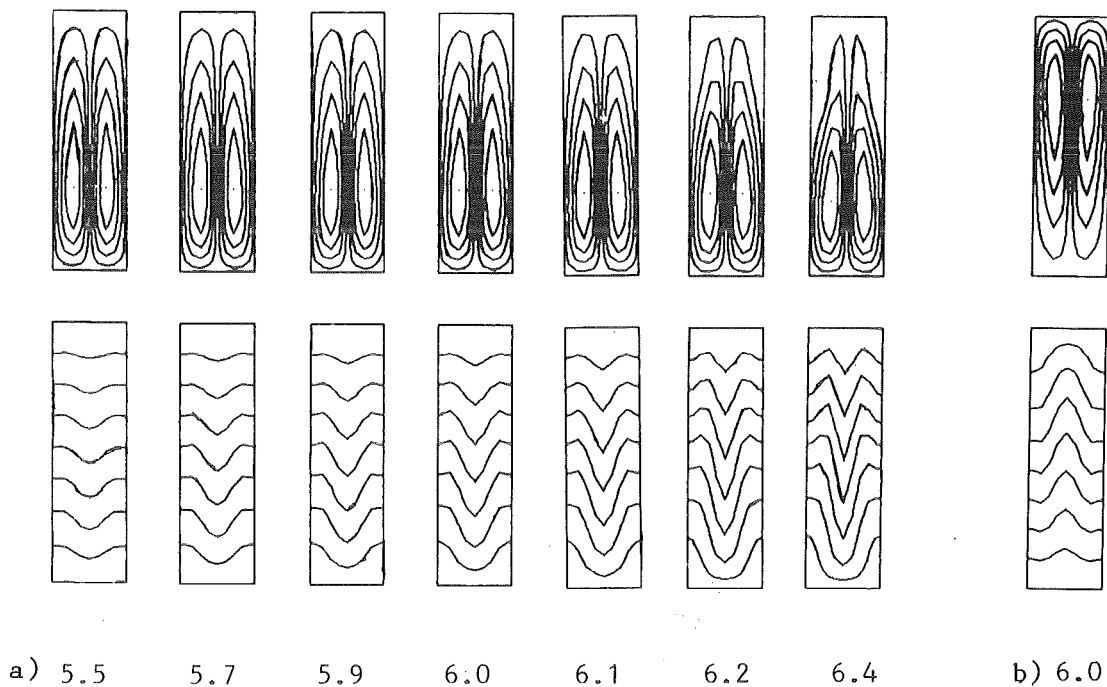a) 5.5   5.7   5.9   6.0   6.1   6.2   6.4   b) 6.0

Fig. 11   Steady-state double roll convection, mode 6, streamline and isotherm patterns for increasing Rayleigh numbers
a) downflow along the vertical center line,
b) upflow along the vertical center line.

The heat transfer rate, in contrast to that used previously, is characterized by the mean Nusselt number $\overline{Nu}$ at the lower boundary. The rates due to modes 1, 2, and 6 are displayed in fig. 12. The transition between the steady mode 1 and the oscillatory mode 2 is indicated in the graph by a sudden change in the slope of the $\overline{Nu}$(Ra)-curve at the second critical Rayleigh number. (The solid line represents an interpolation curve through several calculated values $\overline{Nu}$(Ra)). The Nusselt number seems to vary continuously in the neighbourhood of Ra_{c2}.

- Large Sidewalls, Finite Conductivity
For a more realistic simulation of the thermal boundary conditions of the experiments we conduct some computations for two more cases, namely, the large side walls of the cell have a finite conductivity while the small side walls are either adiabatic or perfectly conducting. These computations are

particularly aimed at exploring the transition from the steady single roll
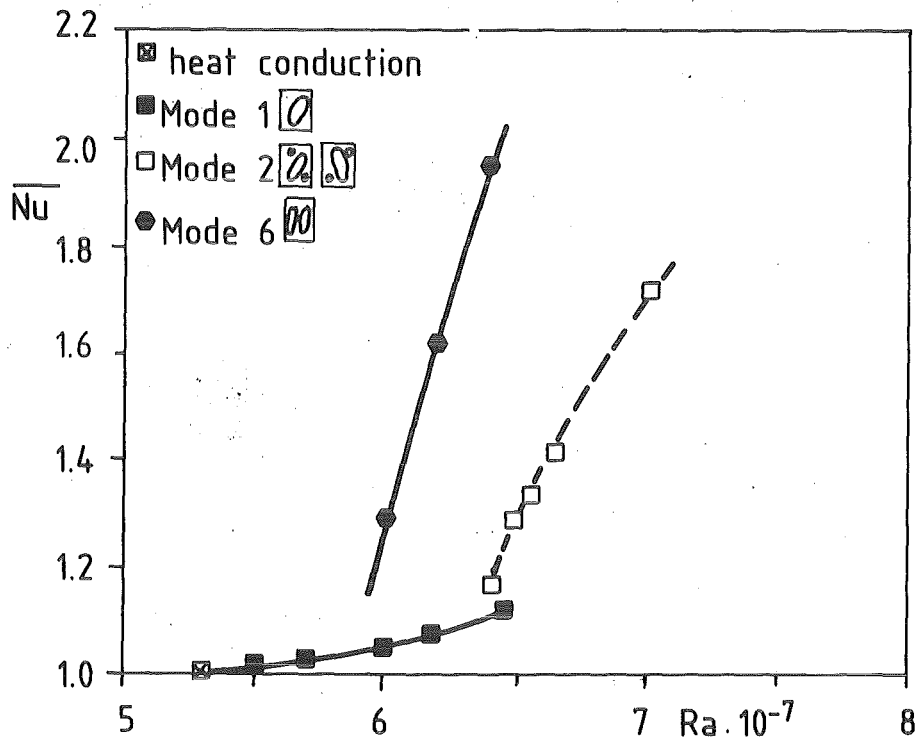convection mode 1 to more complicated modes as affected by the conductivity
parameter H.

Fig. 12   Time averaged Nusselt number versus Rayleigh number, symbols repre-
          sent calculated values, solid curves are fitted to the calculated
          values, perfectly conducting large sidewalls, adiabatic small side
          walls

We find that the single roll mode may be replaced by the oscillatory mode 2
(the diagonal oscillation), by mode 6, a steady double roll mode, or by its
oscillatory manifestation depending on the value of H and the thermal bounda-
ry conditions of the small side walls. The essential features of this transi-
tion are displayed in figs. 13 and 14. For increasing values of Ra and
adiabatic small side walls (fig. 13) the steady single roll convection deve-
lops into the diagonal oscillation when H is typically in the range $0 \leqslant H \leqslant$
0.2, for larger values of H a steady double roll occurs beyond the dashed
threshold line. We suggest that another dividing line branches off from the
stability curve of mode 1 in the range $0.15 < H < 0.2$ separating the range of
existence of the diagonal oscillation from the range of steady double rolls.
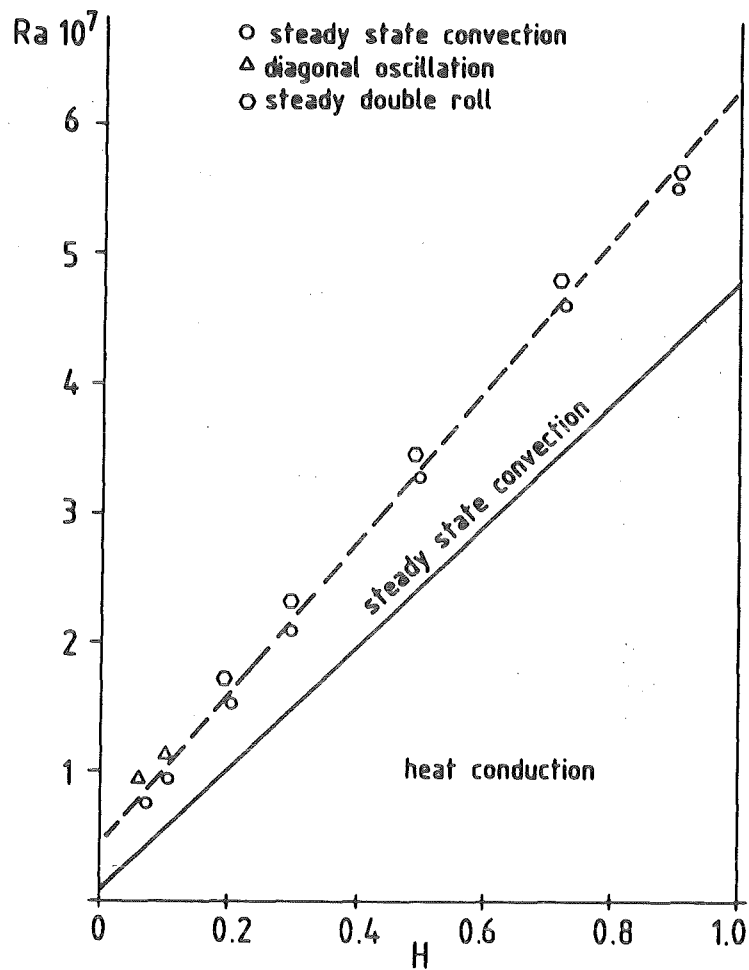
Fig. 13   Regimes of stable flows attained for adiabatic small side walls
dependent on the Rayleigh number Ra and on the thermal coupling
factor H when Ra is increased by small increments of Ra.

We mention here that before transition to oscillatory convection the single
roll mode develops two small vortices in those two opposite corners towards
which the up or downflow is directed. This phenomenon is similar to that
displayed in fig. 9 for the case of perfectly conducting large side walls.

When the small side walls are perfectly conducting the transition to a diago-
nal oscillation, mode 2, occurs again for small values of H in the range 0 < H <
0.2. For larger values of H, typically 0.3 < H < 0.6, the single roll convec-
tion changes into a non-symmetric oscillatory convection which resembles to
some extent still mode 6 for certain time intervalls. The streamlines and
isotherms are displayed in fig. 15. The pattern is periodic in time and so is
the history of the Nusselt number inspite of the spatial non-symmetry of the
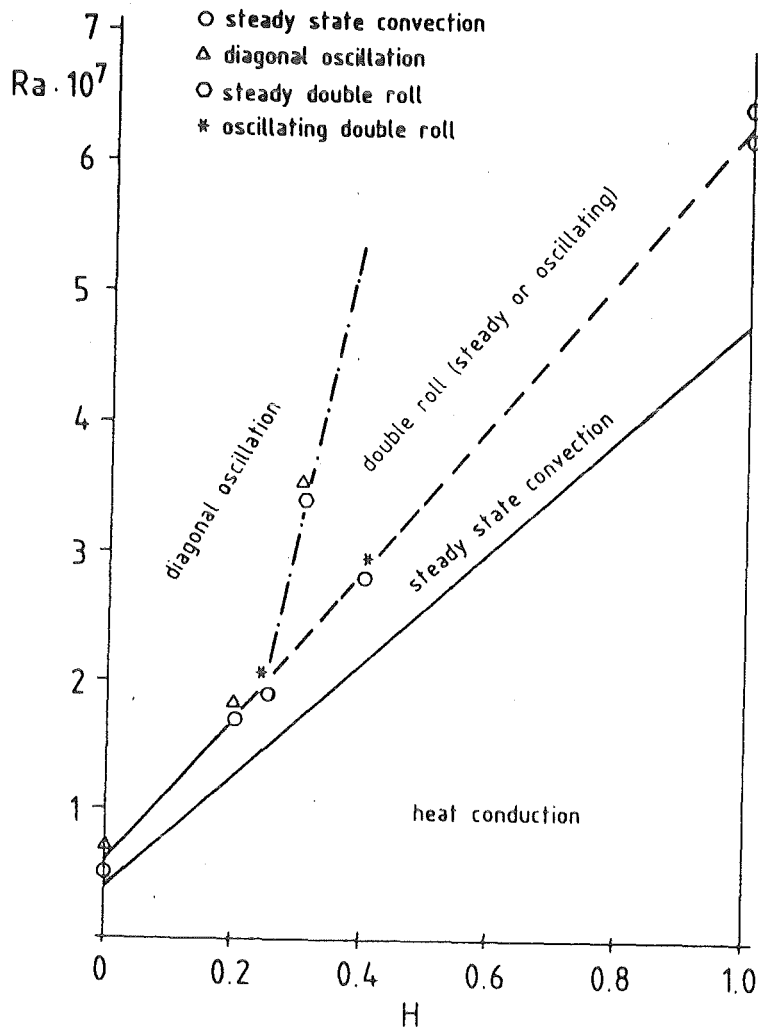pattern. Furtheron we refer to this pattern as mode 6a. We infer from the

Fig. 14   Regimes of stable flows attained for perfectly conducting small side
walls dependent on Ra and H for small positive increments of Ra.

streamline pattern that this oscillatory mode has multiplicity 4. There is
indication that the transition from the time periodic and spacially symmetric
diagonal oscillation, mode 2, to the time periodic and spacially non-symme-
tric double roll oscillation mode 6a is linked to a period doubling process.
We speculate that before period doubling occurs a separation line branches
off from the stability curve for the single steady mode. This line is indi-
cated in fig. 14 by the dashed dotted line. In this case the direction of the
separation line is estimated due to the following numerical finding. For H =
0.30 and Ra = 3.4 x 10^7 a transition from a steady double roll, mode 6, to a
non-symmetric diagonal oscillation, mode 2a, is found. However, we must say
that more detailed calculations are needed to fix finally the separation line

between the states of diagonal oscillations, steady double roll convection and oscillatory non-symmetric double roll convection. Mode 2a is shown in fig. 16 where for H = 0.3 and Ra = 3.20x10^7 streamline, isotherm patterns and the Nusselt number history is given.
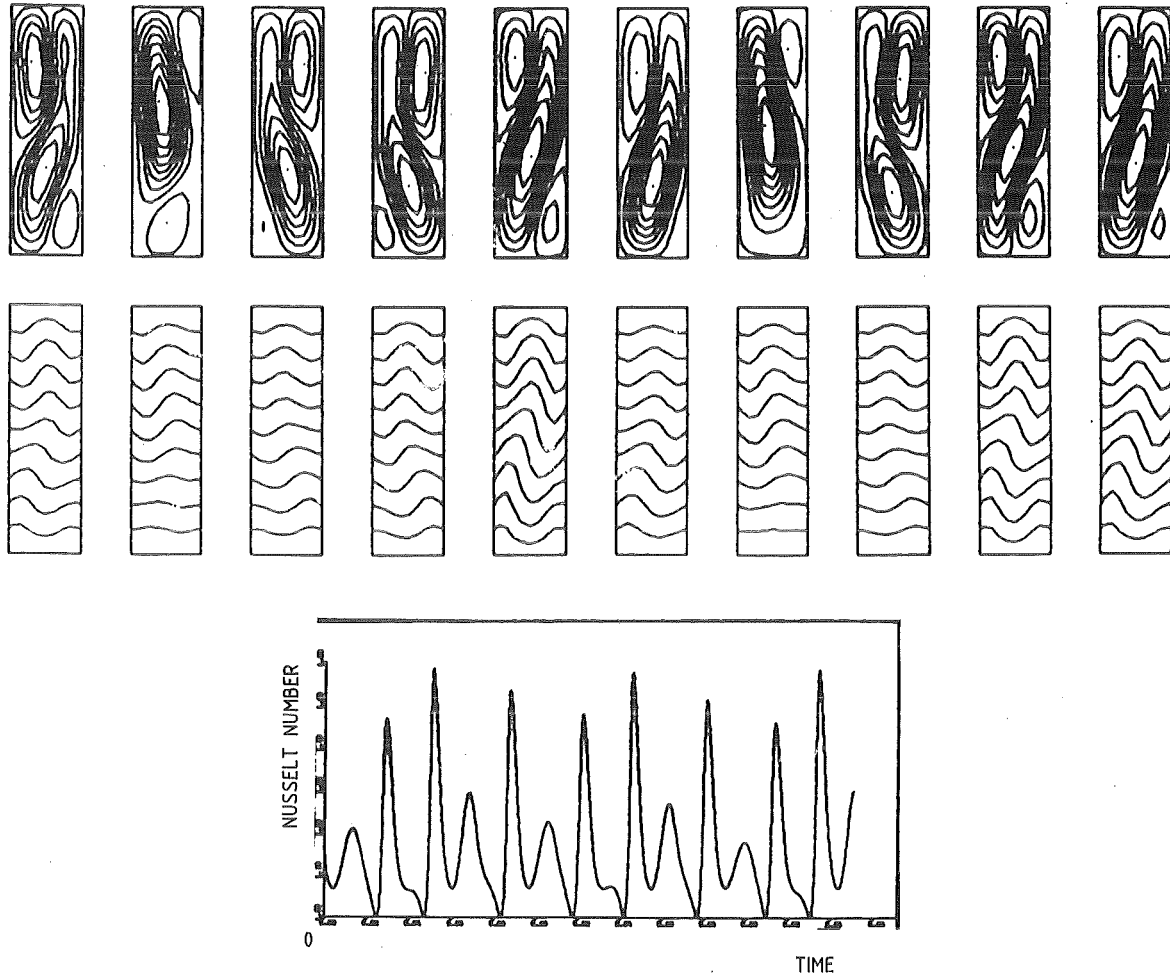
Fig. 15   Oscillatory double roll, mode 6a, Ra = 2x10^7, a) instantaneous streamline and isotherm patterns for two periods of oscillation, perfectly conducting small side walls, H = 0.25, calculation with 9 x 33 points, b) space averaged Nusselt number at the lower side as a function of time.

The oscillatory flow regains more spatial symmetry when H and Ra are increased. This can be seen when H and Ra are increased further for H = 1 and Ra = 6.1x10^7 where we obtain the transition from a steady single roll to a steady double roll (see fig. 14).

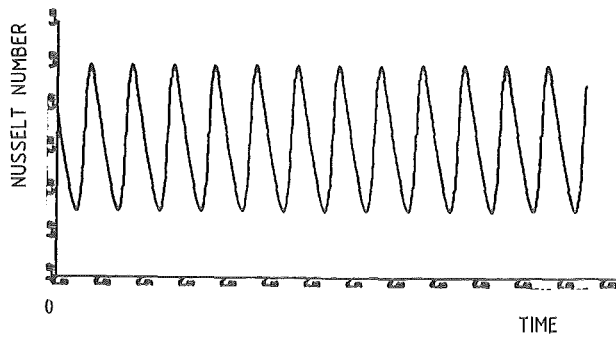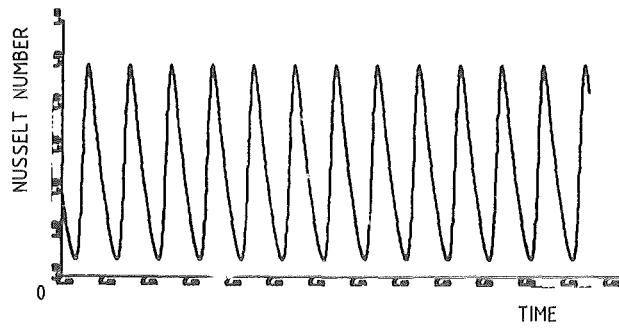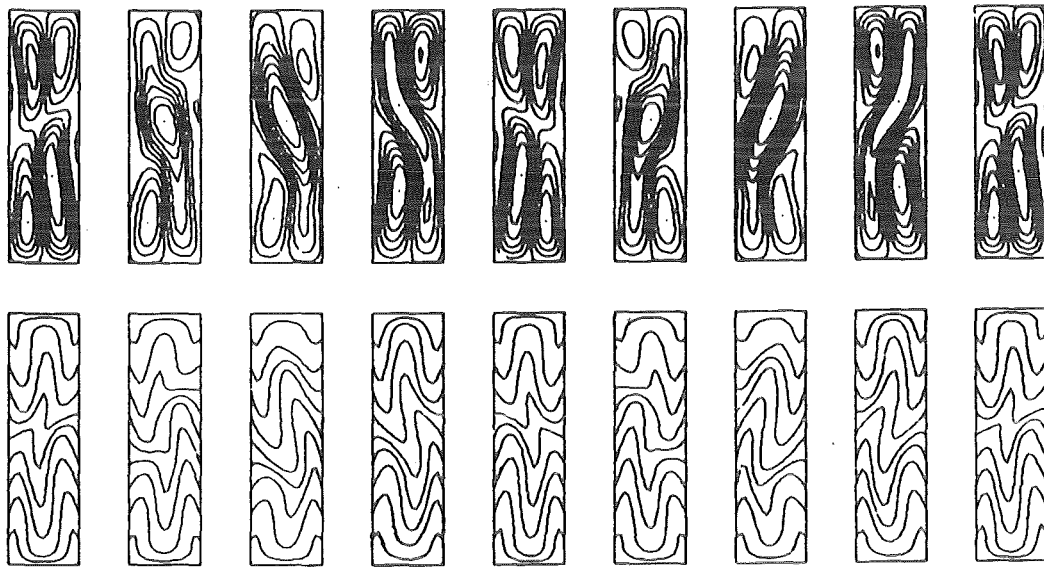Fig. 16 "Non-symmetric diagonal oscillation", Ra = 3.2x10 ^{7}, mode 2a, a) in-
stantaneous streamline and isotherm patterns for one period of
oscillation, perfectly conducting small side walls, H = 0.3,
b,c) the space averaged Nusselt number at the lower and upper side
of the cell.

The period of oscillation is specially determined for mode 2, i.e. the diagonal oscillation and the parameter value H = 0.3. The numerical data are given in fig. 17. In an upscan variation of the Rayleigh number by the amount Δ Ra = 1 x 10^6 the onset of oscillation is observed for Ra = 3.5 x 10^7. A downscan calculation starting from Ra = 4.2 x 10^7 revealed a hysteresis loop since the transition to the steady state single roll model occurs only at Ra = 2.1 x 10^7. The calculated data suggest that there is a distinct change in the slope of the interpolation curve of fig. 17 in the range 2.6 x 10^7 < Ra < 3 x10^7. For Ra $\geqslant$ 3 x 10^7 the interpolation curve is reasonably well represented by a function of the form $\tau^* \sim Ra^{-1.7}$, for Ra < 2.6 x 10^7 a functional dependence of the order $\tau^* \sim Ra^{-8.9}$ can be infered. We mention here that on the downscan path more subtile features of the flow oscillations become apparent in a small range 3.1 x 10^7 < Ra < 3.4 x 10^7. The spatially symmetric diagonal oscillation passes through a nonsymmetric state by first loosing
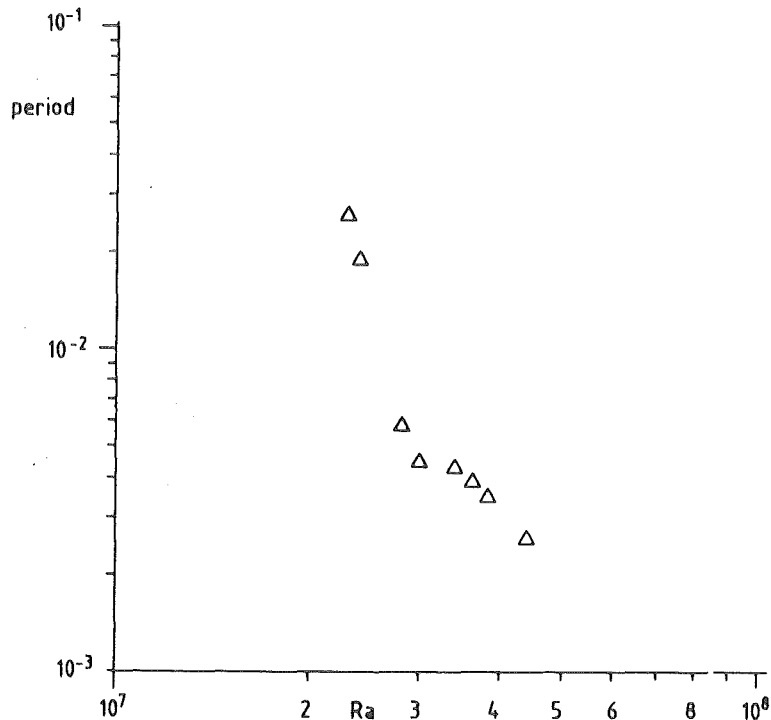
Fig. 17   Dimensionless period τ^* of the diagonal oscillation, mode 2, as a function of Ra for H = 0.3, perfectly conducting small side walls, calculation with 17 x 65 points, time step $\Delta t' = 1.22$ x 10^{-6}.

spatial symmetry in the range 3.4 x 10^7 > Ra > 3.2 x 10^7 and regaining it in the range 3.2 x 10^7 > Ra > 3.1 x 10^7. In this transition process the oscillation remains periodic, however, the histories of the Nusselt numbers at the

bottom and the top of the cell undergo a phase shift[1] (see fig. 18). A
relative change of the amplitudes of the Nusselt numbers is related to this
process.
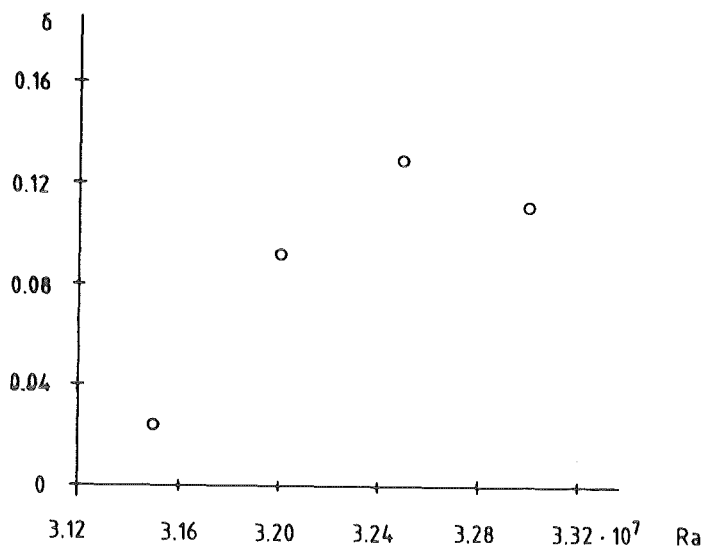
Fig. 18   Angle of phase shift of the "upper" versus "lower" Nusselt number as
           a function of the Rayleigh number Ra for H = 0.3. Calculations with
           a 17 x 65 grid, $\Delta t' = 1.22 \times 10^{-6}$

5   Comparison between numerical and experimental results

We have performed most of our numerical calculations for the limiting thermal
boundary conditions "adiabatic sidewalls" and "perfectly conducting sidewalls".
Since a Hele-Shaw cell prepared for flow visualization in reality has side-
walls of finite heat conductivity, some screening calculations have been
conducted using the thermal boundary condition of the third kind which con-
tains the model Biot number α' . We have adjusted this parameter α' and the
related H to the experimental conditions. Using the geometrical dimensions
and the thermal conductivities of the fluid and wall material the Biot num-
bers for the experimental conditions of Koster & Müller (1984) are roughly
assessed as $\alpha' = 0.5$ in the case of the combination silicon oil as a test
fluid and plexiglas side walls and as $\alpha' = 2.6$ for the combination silicon
oil and glass side walls.

---

[1]   The phase shift between the Nusselt number at the lower and upper side of
       the cell can be seen in fig. 16b and 16c.

In Table 1 the critical Rayleigh numbers are listed for the particular geometry but for various thermal boundary conditions. The table contains the experimental values of Koster & Müller (1984) and our calculated values.
It is known from the Rayleigh-Bénard instability theory that the first critical value of the Rayleigh number increases with the conductivities of the upper and lower boundaries (see e.g. Sparrow et al. (1964)). This trend is seen to hold also for the sidewalls from Table 1 for the first critical Rayleigh number Ra_{c1}. We mention that the calculated values of Ra_{c2} for onset of oscillation as well as the experimental data refer to the oscillatory mode 2. Moreover the data for the upscan variation of the Rayleigh number are listed for comparison.

In general we consider the agreement between calculated values and experimental findings as resonably good, if one keeps in mind that the onset of oscillation is influenced by a hysteresis effect.

Boundary conditions at the sidewalls	Ra_{c1} onset of convection	Ra_{c2} onset of oscillation
Calculation: all sidewalls adiabatic $\alpha' = 0$	1.0×10^6	5.9×10^6 upscan
Experiment: all sidewalls of Plexiglas $\alpha' = 0.5$	1.75×10^6	2.78×10^7 upscan
Experiment: small sidewalls of copper, $\alpha' = \infty$, large sidewalls of glass, $\alpha' = 2.6$	1.3×10^7	4.9×10^7 upscan
Calculation: small sidewalls perfectly conducting, $\alpha' = \infty$, large sidewalls of finite conductivity $\alpha' = 2.6$	1.3×10^7	3.4×10^7 upscan
Calculation: small sidewalls perfectly conducting, $\alpha' = \infty$, large sidewalls of finite conductivity $\alpha' = 2.6$	1.3×10^7	2.2×10^7 downscan
Calculation: small sidewalls adiabatic, $\alpha' = 0$, large sidewalls perfectly conducting, $\alpha' = \infty$	4.4×10^7	5.4×10^7 upscan

Table 1: Calculated and experimentally determined critical Rayleigh numbers.

Lyubimov et al. (1977) have conducted a similar study on convective flow in a Hele-Shaw cell of aspect ratio h/b = 2. They claim that they were able to predict their experimentally observed critical Rayleigh numbers for onset of convection and in particular for onset of oscillation to within 5 % accuracy. They employ a Galerkin method retaining eigenfunctions of the linear problem of index order $N \leq 4$ in their expansion. They do not account for the finite conductivity of their sidewalls in their calculations. Recently McLaughlin & Orszag (1982), Strauß & Schubert (1981, 1986), Curry et al. (1984) have demonstrated that accurate predictions for unsteady thermal convection by spectral methods need eigenfunction expansions of an index order much larger than $N \leq 4$. They use typically between 8 and 32 functions for the resolution in one spatial direction. In the light of these theoretical results and moreover the possibility of experimental errors the good agreement claimed by Lyubimov at al. (1977) may be questioned.

Next we compare our calculated period of oscillation at the beginning of oscillation with the values measured by Koster & Müller (1984) for various thermal conditions at the sidewalls of the Hele-Shaw cell

Table 2 shows that according to our calculations adiabatic sidewalls exhibit the longest period of oscillation while perfectly conducting sidewalls result in an order of magnitude smaller period for the particular geometry and test fluid chosen. The calculated data compare reasonably well with the measured values obtained for high-conductivity and low-conductivity sidewalls.

We ascribe the remaining differences between the calculated and the measured values of τ^* mainly to the different thermal boundary conditions at the sidewalls. Numerical inaccuracies of the calculated periods are found to be of the order $\Delta\tau^*/\tau^* \approx 10^{-1}$. (More details about the numerics will be given in the appendix.) More thorough experimental and analytical work is required to clarify the details of the hysteretic behaviour of the oscillation period.

Next we shall relate the calculated streamline and isotherm patterns of the different modes to observations in experiments. These discussions will be mainly qualitative in nature. We mention beforehand that most of the modes found in our calculations have been observed in experiments, although not all in one particular set-up and not for the particular aspect ratio and the particular properties on which our calculations are based.

Boundary conditions at the sidewalls	dimensionless period at onset of oscillation
calculation: all sidewalls adiabatic, $\alpha' = 0$	$\tau^* = 2.6 \times 10^{-2}$
experiment: small sidewalls of PVC, $\alpha' = 0.5$ large sidewalls of Plexiglas, $\alpha' = 0.5$	$\tau^* = 9.1 \times 10^{-3}$
experiment: small sidewalls of copper large sidewalls of glass, $\alpha' = 2.6$	$\tau^* = 3.05 \times 10^{-3}$
calculation: small sidewalls perfectly conducting large sidewalls of finite conductivity $\alpha' = 2.6$	$\tau^* = 4 \times 10^{-3}$
calculation: small sidewalls adiabatic, $\alpha' = 0$ large sidewalls perfectly conducting, $\alpha' = \infty$	$\tau^* = 3.9 \times 10^{-3}$

Table 2: Calculated and experimentally determined period of oscillation at the onset of oscillation in mode 2.

Lyubimov et al. (1977) report (their figure 3) that they find in a Hele-Shaw cell of aspect ratio $h/b = 2$ oscillatory convection of the type mode 2, i.e. the symmetric 3-4 vortex system. They visualize the flow pattern by using tracers in a Hele-Shaw cell with one metallic and one transparent large side wall. They claim that the same pattern is also established and observed by thermocouple readings in a cell with metallic sidewalls. The mode 2 is also observed by Putin & Tkacheva in Hele-Shaw cells of aspect ratio 2 with plexiglas sidewalls and different depths of the gap (their fig. 3). The same authors have realized (their fig. 2) the oscillating double roll mode displayed in fig. 11.

Koster & Müller (1979, 1984) find oscillatory convection of mode 2 in Hele-Shaw cells of aspect ratio h/b = 4.7, 3.5, 1.7 and for various thermal conditions at the sidewalls. They realize, moreover, that the symmetric mode 2 is preferred and more stable in Hele-Shaw cells with high conductivity sidewalls. This supports our numerical findings of section 5, namely that in the case of perfectly conducting sidewalls mode 2 seems to be the only existing oscillatory state in the range of Rayleigh numbers investigated.

Putin & Tkacheva (1979) report the development of the steady single-roll convection, mode 1, with increasing Rayleigh numbers. They observe that the single roll gets tilted to one or the other side of their test cell depending on the history of the heat up. Moreover they visualize recirculation zones in two opposite corners of the cell very similar to those to be infered from the streamline patterns of mode 1 in figs. 2 and 9.

The oscillatory mode 5, consisting of two vortices in vertical order, has been observed by Koster & Müller (1979) in a Hele-Shaw cell of aspect ratio h/b = 4.7 and h/b = 7 and with high conductivity sidewalls. Detailed measurements of the temporal behavior of this mode for further comparison are still missing.

These authors also succeeded in realizing experimentally the steady double roll system mode 6 in Hele-Shaw cells of aspect ratios h/b = 7, 4.7, 3.5. In their system mode 6 undergoes a transition to mode 2 in a cell of h/b = 3.5 and high conductivity sidewalls. When the Rayleigh number is increased, beyond a certain critical value mode 2 proves to be more stable than mode 6 for high values Ra.

The nonsymmetric oscillatory modes 3 and 4 could not be directly identified from experimental findings. Nevertheless, the following general observation of Koster & Müller (1984) supports their existence in real physical systems. Koster & Müller (1984) find a strong tendency for the oscillatory convection to become nonsymmetric in a Hele-Shaw cell with low conductivity sidewalls. This nonsymmetry can be recognized from their interferograms representing the isotherms of the particular convection. These isotherms have some common features with the calculated isotherm fields of modes 3 and 4 in figs. 4 and 5 and of mode 2a and 2b in figs. 15 and 16.

6 Further Reduction of the Model Equation

We now investigate the extent of which special terms in the momentum equations (4a) influence the numerical results. The calculations are carried out for the case of adiabatic sidewalls, a spatial grid of 9x33 mesh points and the standard time step $\Delta t*$[1].

For high Prandtl numbers the inertial terms in the momentum equations can be neglected. We rescale the pressure in equation (12a) and obtain

$$-\nabla_o p + \nabla_o^2 \underset{\sim}{U} - \frac{1}{K^*} \underset{\sim}{U} + Ra \cdot \hat{T} \cdot \underset{\sim}{e}_y = \underset{\sim}{0} \, . \qquad (16)$$

These equations are solved numerically together with the continuity equation (12b), the energy equation (12c) and the boundary condition (14) for H = 0. The calculation is carried out either by increasing the Rayleigh number in small steps and then continuing the calculation until a new permanent solution is established or by starting from a previously found solution of the complete set of equations (12) as an initial condition.

The main results obtained are as follows:
- All convective modes found for the complete set of equations (12) and the same thermal boundary condition could be realized; no additional permanent solutions are detected in the particular range of Rayleigh numbers under investigation.
- The values of the mean Nusselt numbers deviate only insignificantly from those calculated from the original equations.

These results are displayed in fig. 19.

A drastic change in the quality of the numerical equilibrium solutions is noticed when, in addition to the "high Prandtl-number" assumption the equation (16) is further reduced by dropping the viscous terms $\nabla_o^2 \underset{\sim}{U}$. In this case the momentum equations for the Hele-Shaw cell are approximated by the Darcy-equations (see Scheidegger 1972) in the form

$$\nabla_o p - \frac{1}{K^*} \underset{\sim}{U} + Ra \cdot \hat{T} \cdot \underset{\sim}{e}_y = \underset{\sim}{0} \, . \qquad (17)$$

---

1) We used a standard nondimensional time step $\Delta t^* = 3.1 \times 10^{-6}$ and a standard grid of 9 x 33 points if not otherwise stated.
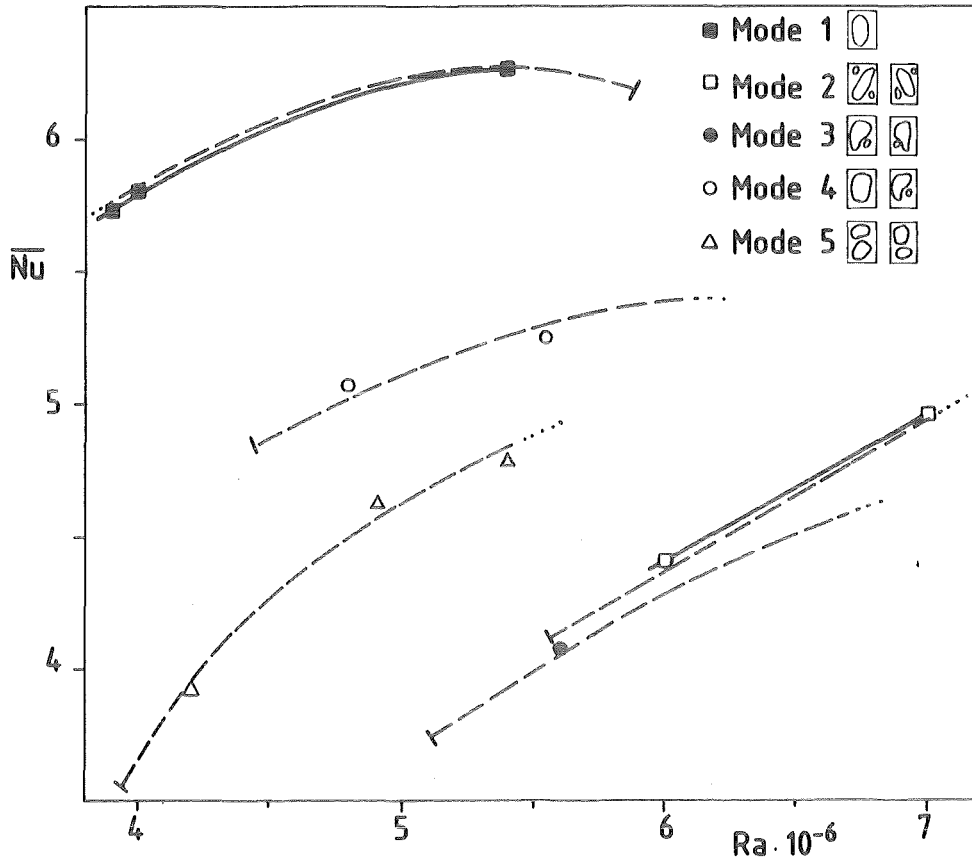
Fig. 19 Time averaged Nusselt numbers versus Rayleigh numbers, inertial
terms neglected in the momentum equations; adiabatic sidewalls
————— inertial terms neglected, ——— inertial terms included.

This approximation requires slip conditions at the small vertical and hori-
zontal boundaries of the Hele-Shaw cell. Figure 20 indicates that it is impor-
tant to incorporate the viscous friction term in the model. There is nearly
no difference of the velocity distribution in the interior of the cavity.
Near the small side walls, however, a viscous boundary layer is established
which comprises more than one computational mesh size Δx and Δy respective-
ly. The quasi-porous flow without viscous friction lacks this boundary layer
as this flow has only a vanishing velocity component normal to the wall.

The numerical results based on equations (12) and (17) lead to the following
conclusions:
- Mode 1 and mode 2 can be obtained.
- Modes 3, 4 and 5 cannot be generated numerically.
- There is a smooth transition from the steady mode 1 to oscillatory flow,
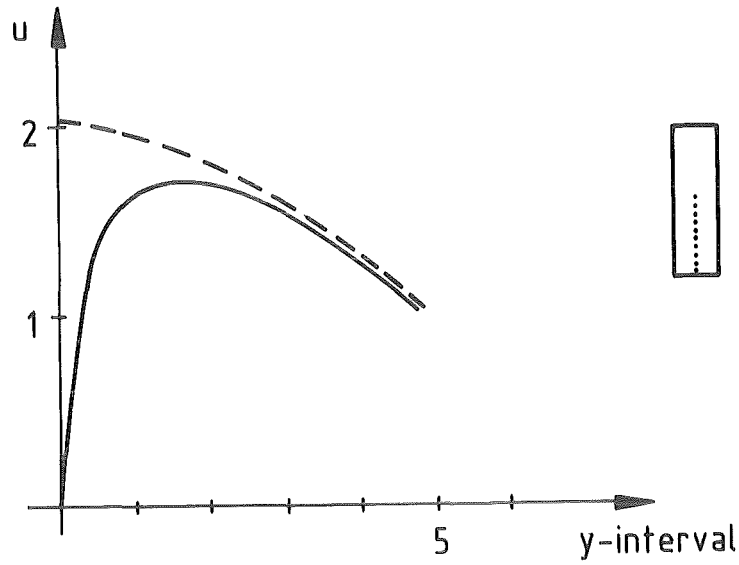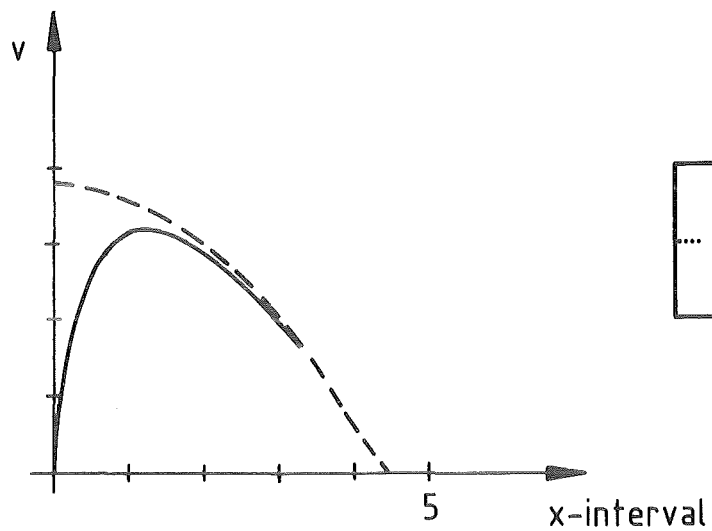
Fig. 20   Effect of the "viscous" and "quasi-porous" friction term on the
velocity distribution in the cell.

a) Velocity component U along the dotted line (see sketch at the
right side) without viscous friction (upper dashed line) and with
viscosity for a weakly supercritical steady flow, Ra = 1.5 x 10^6,
adiabatic walls. U is plotted for the five y-intervalls near the
bottom of the cavity.

b) The component V along the horizontal centerline beginning at the
left vertical wall.

whose streamline and isotherm pattern have the character of mode 1 (see fig. 21). This oscillatory mode is termed mode 1a. The transition occurs at a critical Rayleigh number $Ra_{c2} = 6.6 \times 10^6$.

- Starting from mode 1, mode 2 can only be established by varying the Rayleigh number by a larger step, typically $\Delta Ra = 5.0 \times 10^5$.

- The mean values of the Nusselt numbers are higher than those of the original case.

- Mode 6 can be realized by using as initial conditions even values far from the permanent pattern of mode 6.
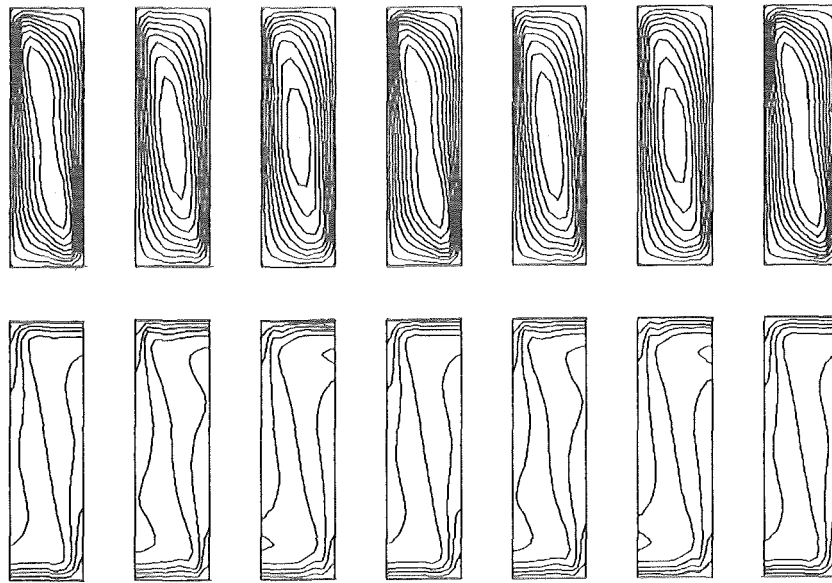
Fig. 21   Oscillatory single roll convection, $Ra = 6.8 \times 10^6$, instantaneous streamline and isotherm patterns for about 2 periods of oscillation, viscous terms in the momentum equations approximated by a Darcy type relation, adiabatic sidewalls.

The range of existence of the modes 1, 1a and 2 is shown in fig. 22.

As a result of these investigations, we conclude that the use of Darcy's approximation for the flow in Hele-Shaw cells of small aspect ratio leads to an unrealistic restriction of the diversity of flow patterns and to physically inaccurate predictions of the heat transfer rates even at moderatly supercritical Rayleigh numbers.
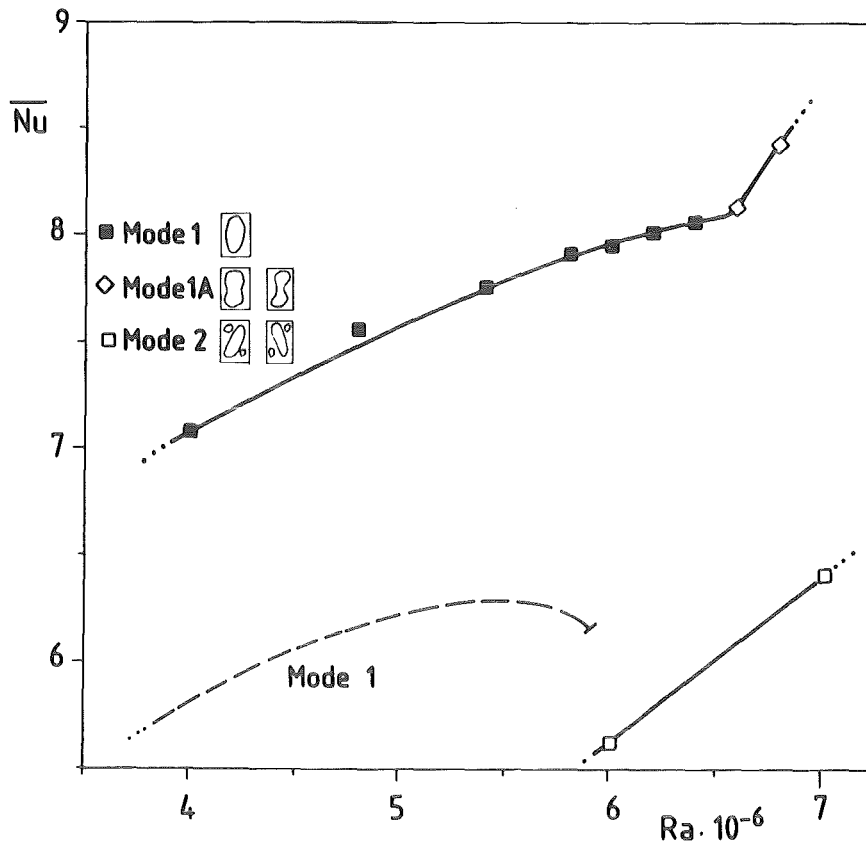
Fig. 22   Time averaged Nusselt number versus Rayleigh number, viscous terms
          in the momentum equations approximated by a Darcy type relation,
          adiabatic sidewalls, ———— Darcy approximation, ——— viscous terms
          included.

7   Summary

By using a simplified form of the Boussinesq equations and a finite dif-
ference scheme we calculate the free convective flow in a Hele-Shaw cell of
small aspect ratio $h/b = 3.5$.

The screening computations are performed for insulating and perfectly conduc-
ting side walls and furthermore for walls of finite conductivity. Six diffe-
rent solutions (modes) are obtained in a transition region from steady to
periodic convection. For insulating sidewalls the multiplicity of permanent
solutions proves to be higher (5 modes) than for perfectly conducting side-
walls (2 modes). This phenomenon is attributed to the symmetrizing effect of
sidewalls of high thermal conductivity. The different modes discovered from
calculations agree qualitatively with experimental observations of streamline

and isotherm patterns of Putin & Tkacheva (1979) and Kester & Müller (1979, 1980, 1984). Furthermore, the calculated critical Rayleigh numbers for onset of convection and onset of oscillation for the two limiting cases insulating and perfectly conducting sidewalls form lower and upper bounds to the experimental data for sidewalls of finite conductivity. We have obtained reasonable agreement between the calculated and the experimentally determined period of oscillation of the symmetric oscillatory mode 2 in the neighbourhood of the transition Rayleigh number. More detailed experimental and analytical work is required to clarify the time behaviour of the system at these branching points. If the viscous terms in the Boussinesq equation are replaced by an approximation of the Darcy type only, essential phenomena of the convective flow in Hele-Shaw cells of small aspect ratio cannot be described. In particular the multiplicity of the equilibrium solution is drastically reduced and the transition to oscillatory convection occurs smoothly in form of a vaccillation of the large vortex mode 1.

Appendix A:

In the relevant two-dimensional domain of the (x,y)-plane a "staggered" grid of constant mesh size is established. Discrete values of the pressure and the temperature are allocated to the center of each mesh while the values of the velocity components are placed in the middle of each mesh side. The finite difference method used is an explicit, fractional time step method for the dependent variables U, V, T. It is essentially based on Leith's one-step, two level, second order accurate difference approximation of the advective terms (see Roache, 1972, p. 75 ff). The pressure is first determined at a point of time $t + \Delta t/2$ by solving a Poisson equation for the pressure using values of U, V, T at time t. A fast solver for the Poisson equation first developed by Swarztrauber and Sweet (1975) is employed to calculate the solution of the pressure equation. In a following step U, V, T are calculated from the difference approximation of the equations (14)-(16) at a time $t + \Delta t$.

To assure stability of the finite difference scheme several conditions are to be satisfied at each grid point:

a) the Courant-Friedrichs-Levy-conditions $c_x \leq 1$, $c_y \leq 1$, where

$$c_x = |U| \frac{\Delta t}{\Delta x} , \quad c_y = |V| \frac{\Delta t}{\Delta y} , \qquad (20a)$$

b) a cell Reynolds number condition which has a somewhat complicated form in relation to the fractional time step method and the Leith's method (see Roache, 1972),

c) a diffusion limit requirement for each equation, the special form of which depending on the structure of the equation. This is outlined here only for a momentum equation which contains two frictional terms giving rise to a stability condition of the form

$$\nu \cdot \Delta t \left\{ \frac{1}{\Delta x^2} + \frac{1}{\Delta y^2} + \frac{6}{d^2} \right\} \leq \frac{1}{2} . \qquad (20b)$$

For the actual physical situation the diffusion stability limit based on the kinematic viscosity proves to be the limiting condition for the time step.

The calculations are performed for a fixed geometry i.e. for fixed aspect ratios h/b, h/d and for a constant Prandtl number. The Rayleigh number is varied. The computations are started from a state of pure heat conduction in which the Rayleigh number is subcritical.

The Rayleighnumber is then increased or decreased instantaneously by small amounts according to the experimental procedure of Koster & Müller (1984) who change the temperature difference between top and bottom of their Hele-Shaw cell quasi-steady.
For continuing the calculations at an increased Rayleigh number as an initial state the previously computed permanent state is chosen. For each change of the Rayleigh number the corresponding permanent solution is calculated. The permanent steady state is considered achieved when the local values of the Nusselt number $\overline{Nu}$ by less than 10^{-3} for a converged run.

The computations could also be restarted for fixed Rayleigh numbers if higher computational accuracy is required; for instance in special cases the mesh size and the time step had to be decreased for increasing Rayleigh numbers and restarts became necessary.

Generally the computations are performed in a rectangular mesh geometry of 9 and 33 grid points in x and y directions. The quality of the computational results is scrutinized in a number of cases by comparing them to runs using a mesh of 18x65 and 36x129 grid points.

For characterizing the permanent solutions of the convective flow the Nusselt number as well as the streamline and isotherm pattern are used.

The local value of the Nusselt number in the grid points is at the lower and upper boundary is defined by the relation:

$$Nu_b^i = \left. \frac{\partial T}{\partial y} \right|_{x=i\Delta x,\ y=0}$$

$$Nu_t^i = \left. \frac{\partial T}{\partial y} \right|_{x=i\Delta y,\ y=1} \quad .$$

(21)

The derivatives with respect to y are obtained from aquadratic approximation of the temperature near the wall, which utilizes three non-equidistant grid points next to the boundary.

The arithmetic mean of all local values Nu_b^i and Nu_t^i at the bottom and top of the domain gives the averaged Nusselt number. The evaluation formula for the lower horizontal boundary then reads

$$Nu_b = \frac{1}{M} \sum_{i=1}^{M} Nu_b^i .$$

(22)

A corresponding relationship holds at the upper horizontal boundary. For time dependent solutions the Nusselt number varies in time. We approximate the time-averaged Nusselt number for periodically varying convection by taking the arithmetic mean of the maximal and minimal value of $Nu(t)$, i.e.

$$\overline{Nu} = \frac{1}{2} [Nu_{max} + Nu_{min}] .$$

(23)

For displaying the pattern of the convective flow the instantaneous streamline and isotherm fields are plotted for consecutive time steps.

Discussion of the accuracy of the numerical results.

We usually expect the calculated solutions of differenc equation to converge towards the solutions of the related differential equat:on if the time and length steps are reduced provided the difference approximations are consistent and numerical stability conditions are met.

The results of chapter 4 are scrutinized by repeating the calculations as well for smaller mesh sizes Δx and Δy as for smaller time steps Δt. Since we use an explicit numerical scheme and since the computations were performed close to its stability limit, a reduction of the mesh sizes generally require a simultaneous reduction of the time step.

In order to separate the effects of varying the mesh size and the time step we first investigate the effects due to reducing the time step only.

For assessing the quantity of the effects we recalculate and compare the range of stability of the different flow patterns, the averaged Nusselt number $\overline{Nu}$ and the nondimensional period of oscillation $\cdot^*$ for different Δx, Δy and Δt.

I – Effect of smaller time steps

The equations (3.16) are solved for the case of adiabatic side walls employing the standard mesh size with 9 x 33 grid points, however, reducing the standard time step $\Delta t^* = 3.1 \times 10^{-6}$ to values of $\Delta t^*/2$, $\Delta t^*/4$, $\Delta t^*/8$ and $\Delta t^*/16$.

The following results are obtained:

– All the various flow patterns are obtained also for the smaller time steps. However, the critical Rayleigh numbers related to the pattern transitions shift monotonically to smaller values indicating a finite lower limit.

- Smaller time step sizes result in higher Nusselt numbers. The values seem to converge monotonically to an upper limit with decreasing time steps. This can be seen from table A1.

time step	$\overline{Nu}$
Δt^*	5.91
$\Delta t^*/2$	6.33
$\Delta t^*/4$	6.54
$\Delta t^*/16$	6.71

Table A1: Variation of $\overline{Nu}$ dependent on the time step Δt for the steady single roll pattern at $Ra = 4.2 \times 10^6$ and a 9 x 33 grid.

A brief comment is given concerning this dependency of the Nusselt number on the size of the time step.

Several standard algorithms designed to solve numerically advection-diffusion equations calculate a steady solution independent of Δt using time marching procedures. This is not the case when the method of Leith is used for approximating the inertial terms. This is described in some detail by Roache (1972) in his book on computational fluid dynamics (p. 357). He derives an error term of the order $u^2 \Delta t/2$ for a steady solution of the momentum transport equation employing the Leith method. Furthermore, we calculate the pressure from a Poisson equation, the inhomogeneous term of which contains a corrective term to account for the conservation of mass. This term is inversely propotional to Δt. Therefore a weak dependence of the steady state solution on the time step is to be expected due to the particular numerical method used.

The influence of the time step on the period of oscillation for different Rayleigh numbers and flow pattern can be seen in table A2. We conclude, that the standard time step Δt^* is relatively large and that the values for smaller time steps increase monotonically by non negligible amounts. However, one may infer from a particular sequence of τ^*-values convergence to an upper limit.

Ra	Δt^*	$\Delta t^*/2$	$\Delta t^*/4$	$\Delta t^*/8$
$4.2 \cdot 10^6$ (mode 5)	2.98	4.74		
$6 \cdot 10^6$ (mode 2)	2.30	2.65	2.79	2.86
$7 \cdot 10^6$ (mode 2)	1.67	1.91	2.03	2.11
$8 \cdot 10^6$ (mode 2)	1.33	1.55 (at $\Delta t^*/3$)		

Table A2: Effect of time step size on the calculated period of oscillation. The table gives the value of $100 \cdot \tau^*$.

II - Effect of mesh size

Employing a fixed time step of $\Delta t^*/16$ but different mesh sizes calculations are performed for a fixed Ryleigh number Ra = 4.2×10^6 and the particular pattern of mode 1. The boundary conditions are the same as in the previous case i.e. adiabatic side walls. The reduction of the mesh size results in monotonically decreasing Nusselt numbers. This can be recognized from table A3. Convergence to an lower limit for $\Delta x \rightarrow 0$ and $\Delta y \rightarrow 0$ is indicated by the sequence of values. Further investigations concerning the range of validity of the range of numerical existence of the various modes are renounced with because of high computationals costs.

Ra = $4.2 \cdot 10^6$, steady state single roll, $\Delta t = \dfrac{\Delta t^*}{16}$	
mesh	$\overline{Nu}$
9 * 33	6.72
18 * 65	6.18
36 * 129	6.08

Table A3: Averaged Nusselt number $\overline{Nu}$ for the steady state single roll for different mesh sizes.

III - Combined effect of variation of time step and mesh size

The combined effect of mesh size and time step variation on the range of existence of the different modes is investigated by choosing numerical values Δx, Δy and Δt in such a way that the stability parameter

$$d^* = \varkappa \frac{\Delta t}{\Delta x^2 + \Delta y^2}$$

which is similar to the parameter of equation (20b), remains fixed. Computer runs are performed for grids with 9 x 33 points and time step Δt^* as well as for 18 x 65 mesh points and time step $\Delta t^*/4$. The results are displayed in figure A1.

Figure A1 shows, that all the various flow patterns termed modes 1 - 5 are obtained as stable equilibrium solutions. Generally minor changes were found regarding the upper or lower bounds of existence of the different modes.

More pronounced discrepancies occur at the lower bound of existence of mode 2 i.e. the so called diagonal oscillatory convection and at the upper stability limit of mode 4. These stability limits differ considerably if the number of grid points is changed from 9 x 33 to 18 x 65 (see figure A1). Also the differences in the values of Nu suggest that the grid with 9 x 33 points has been to coarse to yield quantitatively correct values.
Moreover all calculated values of the Nusselt number are higher for the 18 x 65 grid, with the time step $\Delta t^*/4$.

The combined effect of time step and mesh size variation on the period of oscillation τ^* for different modes can be seen from table A4.

Generally we may state here, that a refined computation by doubling the number of spacial grid points and by reducing the time step by a factor 1/4 still results in small variations in the Nusselt Rayleigh number graph. However, as far as the convection patterns are concerned no qualitative change of the overall behaviour is observed.
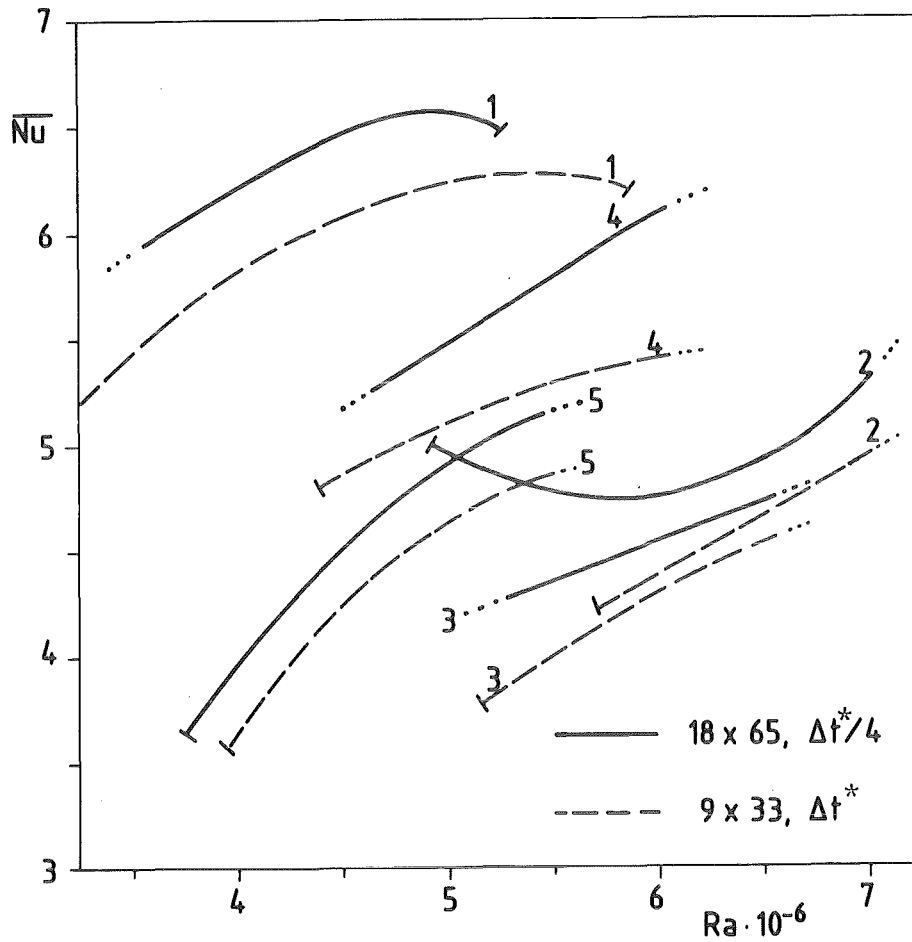
Fig. A1: Averaged Nusselt number versus Rayleigh number;
results for a 9 x 33 point grid and $\Delta t^* = 3.1 \times 10^{-6}$
results for a 18 x 65 point grid and $\Delta t^*/4$

9 * 33 grid points, Δt^*		18 * 65 grid points, $\frac{\Delta t^*}{4}$	
Ra	$\tau^* \cdot 100$	Ra	$\tau^* \cdot 100$
$4.5 \cdot 10^6$ (mode 5)	2.52	$4.5 \cdot 10^6$ (mode 5)	2.48
$5.4 \cdot 10^6$ (mode 5)	1.79	$5.3 \cdot 10^6$ (mode 5)	1.86
$7 \cdot 10^6$ (mode 2)	1.67	$7 \cdot 10^6$ (mode 2)	2.21

Table A4: Combined effect of time step and mesh size variation on the
calculated period of oscillation.

Moreover, we believe that we demonstrated by our numerical analysis the physical phenomena reported in chapter 4 and our conclusions in chapter 5 to be valid and not due to numerical effects.

Literature

Ahlers, G & Behringer, R.P. 1978 The Rayleigh-Benard Instability and Evolution of Turbulence. Supplement of the Progress of Theoretical Physics No. 64, pp. 186-201.

Behringer, R.P. & Ahlers, G. 1982 Heat Transport and Temporal Evolution of Fluid Flow Near the Rayleigh-Benard Instability in Cylindrical Containers. J. Fluid Mech. 125, pp. 219-258.

Behringer R.P., Shaumeyer, J.N., Clark, C.A., Agosta C.C. 1982 Turbulent Onset in Moderately Large Convecting Layers. Physical Review A 26, 3723-3726.

Berge, P. & Dubois, M. 1980 Different Routes to Turbulence in High Prandtl Number Convection and in Rectangular Cells: Influence of the Aspect Ratio and the Structure. In: Systems Far from Equilibrium. Sitges Conference on Statistical Mechanics, June 1980, Editor: Garrido, L., Springer Lecture Notes in Physics 132, pp. 381-394.

Brinkmann, H.C. 1949 A Calculation of the Viscous Force Exerted by a Flowing Fluid on a Dense Swarm of Particles. Appl. Sci. Research, A1, 27-34.

Caltagirone, J.P. 1975 Thermoconvective Instabilities in a Horizontal Porous Layer. J. Fluid Mech. 72, pp. 269-287.

Curry, J.H. Herring, J.R., Longcaric, J., Orszag, S.A. 1984 Order and Disorder in Two- and Three-Dimensional Benard Convection. J. Fluid Mech. 147, pp. 1-38.

Eckmann, J.P. 1981 Roads to Turbulence in Dissipative Dynamical Systems. Reviews of Modern Physics 53, 643-654.

Frick, H. & Müller, U. 1983 Oscillatory Hele-Shaw Convection. J. Fluid Mech. 126, pp. 521-532.

Gollub, J.P. & Benson, S.V. 1980 Many Routes to Turbulent Convection. J. Fluid Mech. 100, pp. 449-470.

Grötzbach, G. 1982 Direct Numerical Simulation of Laminar and Turbulent Benard Convection. J. Fluid Mech. 119, pp. 27-53.

Günther, C. 1981 Numerische Untersuchung der Naturkonvektion in einer von unten beheizten schmalen Hele-Shaw Zelle, Kernforschungszentrum Karlsruhe, KfK 3142/81.

Günther, C. 1982 Zur Identifikation von Lösungsverzweigungen bei der Natur-konvektion in einer von unten beheizten schmalen Hele-Shaw Zelle. Z. angew. Math. Mech. 62, T207-T209.

Hele-Shaw, H.S. 1898 Investigation of the Nature of Surface Resistance of Water and Streamline Motion Under Certain Experimental Conditions. Trans. Inst. Naval Archit., 40. pp. 21-46.

Horne, R.N. & Caltagirone, J.P. 1980 On the Evolution of Thermal Disturbances During Natural Convection in a Porous Medium. J. Fluid Mech. 100, pp. 385-395.

Horne, R.N. & O'Sullivan, M.J. 1978 Origin of Oscillatory Convection in a Porous Medium Heated from Below. Phys. Fluids 21, 1260-1264.

Howard, L.N. 1964 Convection at High Rayleigh Number. 11th Int. Congress on Applied Mechanics. München, H. Görtler ed., Springer, Berlin, pp. 1109-1115.

Kessler, R. 1983 Oszillatorische Konvektion. Dissertation Universität Karlsruhe, West Germany (DFVLR-Rep RB-84-14).

Kessler, R. Nonlinear transition in three-dimensional convection. J. Fluid Mech. 174, 357-379 (1987)

Kimura, S. & Schubert, G. 1986 Route to chaos in porous media thermal convection. J. Fluid Mech. 166, pp. 305-324.

Koster, J.N. & Müller, U. 1980 Free Convection in Vertical Slots. In: Natural Convection in Enclosures HTD-Vol. 8. The American Society of Mechanical Engineers. United Eng. Center, 345 East 47th Street, New York, 10017, pp. 27-30.

Koster, J.N. & Müller, U. 1979 Vertically Staggered Patterns in Free Convective Flow. In: Recent Developments in Theoretical and Experimental Fluid Mechanics", Ed. U. Müller, K.G. Roesner, B. Schmidt, Springer Berlin, Heidelberg, New York.

Koster, J.N. & Müller, U. 1982 Free Convection in Vertical Gaps. J. Fluid Mech. 125, pp. 429-451.

Koster, J.N. & Müller, U. 1984 Oscillatory Convection in Vertical Slots. J. Fluid Mech. 139, pp. 363-390.

McLaughlin, J.B. & Orszag, S.A. 1982 Transition from Periodic to Chaotic Thermal Convection. J. Fluid Mech. 122, pp. 123-142.

Libchaber, A., Laroche, C., Fauve, S. 1982 Period Doubling Cascade in Mercury, a Quantitative Measurement. Le Journal De Physique-Lettres 43, L-211-L-216.

Libchaber, A., Fauve, S., Laroche, C. 1983 Two-Parameter Study of the Routes to Chaos. Physica 7D, pp. 73-84.

Lipps, F.B. 1976 Numerical Simulation of Three-dimensional Benard Convection in Air. J. Fluid Mech. 75, pp. 113-148.

Lyubimov, D.V., Putin, G.F., Chernatynski, V.J. 1977 On Convective Motions in a Hele-Shaw Cell. Sov. Phys. Dokl. 22, pp. 360-362.

Putin, G.F., Tkacheva, E.A. 1979 Experimental Investigation of Supercritical Convective Motions in a Hele-Shaw Cell. Isvestiya Akad. Nauk SSR, Mekhanika Zhidkosti Gazi, Vol. 14, pp. 3-9.

Rabinovich, M.J. 1978 Stochastic Self Oscillations and Turbulence, Sov. Phys.1 Up. 21, 5, pp. 443-469.

Roache, P.J. 1972 Computational Fluid Dynamics. Hermosa Publishers Albuquerque, New Mexico.

Scheidegger, A.E. 1974 The Physics of Flow Through Porous Media. University of Toronto Press.

Schubert, G. & Strauß, J.M. 1982 Transition in Time-Dependent Thermal Convection in Fluid-Saturated Porous Media. J. Fluid Mech. 121, pp. 301-313.

Sparrow, E.M. Goldstein, R.J. & Jonsson, V.H. 1964 Thermal Instability in a Horizontal Fluid Layer: Effect of Boundary Conditions and Nonlinear Temperature Profile. J. Fluid Mech. 18, 513-528.

Swarztrauber, P., Sweet, R. 1975 Efficient FORTRAN Subprograms for the Solution of Elliptic Partical Differential Equations. Tech. Note NCAR/TN-109+IA National Center of Atmospheric Reserach.

Figure captions

Fig. 1   Principle sketch of a Hele-Shaw cell of small aspect ratio.

Fig. 2   Steady-state single roll, mode 1, streamline and isotherm pattern
          for five different Rayleigh numbers, from Fig. 2a to Fig. 2e read
          $Ra \times 10^{-6} = 1, 1.5, 2, 4, 5$.

Fig. 3   "Diagonal oscillation" or mode 2; $Ra = 6.0 \times 10^{6}$, instantaneous
          streamline and isotherm patterns for one half-period of oscillation,
          adiabatic sidewalls.

Fig. 4   "Vertical oscillation" or mode 3; $Ra = 5.8 \times 10^{6}$, instantaneous
          streamline and isotherm patterns for one period of oscillation,
          adiabatic sidewalls.

Fig. 5   "Non-symmetric oscillation" or mode 4; $Ra = 5.8 \times 10^{6}$, instantaneous
          streamline and isotherm patterns for one half period of oscillation,
          adiabatic sidewalls.

Fig. 6   "Vertical oscillation" or mode 5; $Ra = 5.8 \times 10^{6}$, instantaneous
          streamline and isotherm patterns for one period of oscillation,
          adiabatic sidewalls.

Fig. 7   Time averaged Nusselt number versus Rayleigh number, symbols repre-
          sent calculated values, solid curves are fitted to the calculated
          values, dashed curves indicate transitions between the different
          modes, adiabatic sidewalls.

Fig. 8   Dimensionless period of oscillation versus Rayleigh number.

Fig. 9   Streamline and isotherm pattern of steady-state convection, mode 1,
          perfectly conducting large sidewalls, adiabatic small sidewalls.

Fig. 10   "Diagonal oscillation"; mode 2; $Ra = 6.5 \times 10^{7}$, instantaneous
          streamline and isotherm patterns for more than one period of
          oscillation, perfectly conducting large sidewalls, adiabatic small
          sidewalls.

Fig. 11   Steady-state double roll convection, mode 6, streamline and iso-
          therm patterns for increasing Rayleigh numbers
          a) downflow along the vertical center line,
          b) upflow along the vertical center line.

Fig. 12   Time averaged Nusselt number versus Rayleigh number, symbols repre-
          sent calculated values, solid curves are fitted to the calculated
          values, perfectly conducting large sidewalls, adiabatic small side
          walls.

Fig. 13   Regimes of stable flows attained for adiabatic small side walls
          dependent on the Rayleigh number Ra and on the thermal coupling
          factor H when Ra is increased by small increments of Ra.

Fig. 14   Regimes of stable flows attained for perfectly conducting small side
          walls dependent on Ra and H for small positive increments of Ra.

Fig. 15   "Oscillating double roll", mode 6a, Ra = 2×10^7, a) instantaneous
          streamline and isotherm patterns for two periods of oscillation,
          perfectly conducting small side walls, H = 0.25, calculation with 9
          x 33 points, b) space averaged Nusselt number at the lower side as a
          function of time.

Fig. 16   "Non-symmetric diagonal oscillation", Ra = 3.2×10^7, mode 2a, a) in-
          stantaneous streamline and isotherm patterns for one period of
          oscillation, perfectly conducting small side walls, H = 0.3,
          b,c) the space averaged Nusselt number at the lower and upper side
          of the cell.

Fig. 17   Dimensionless period τ^* of the diagonal oscillation, mode 2, as a
          function of Ra for H = 0.3, perfectly conducting small side walls,
          calculation with 17 x 65 points, time step $\Delta t' = 1.22 \times 10^{-6}$.

Fig. 18   Angle of phase shift of the "upper" versus "lower" Nusselt number as
          a function of the Rayleigh number Ra for H = 0.3. Calculations with
          a 17 x 65 grid, $\Delta t' = 1.22 \times 10^{-6}$

Fig. 19 Time averaged Nusselt numbers versus Rayleigh numbers, inertial terms neglected in the momentum equations; adiabatic sidewalls ——— inertial terms neglected, --- inertial terms included.

Fig. 20 Effect of the "viscous" and "quasi-porous" friction term on the velocity distribution in the cell.
   a) Velocity component U along the dotted line (see sketch at the right side) without viscous friction (upper dashed line) and with viscosity for a weakly supercritical steady flow, $Ra = 1.5 \times 10^6$, adiabatic walls. U is plotted for the five y-intervalls near the bottom of the cavity.
   b) The component V along the horizontal centerline beginning at the left vertical wall.

Fig. 21 Oscillatory single roll convection, $Ra = 6.8 \times 10^6$, instantaneous streamline and isotherm patterns for about 2 periods of oscillation, viscous terms in the momentum equations approximated by a Darcy type relation, adiabatic sidewalls.

Fig. 22 Time averaged Nusselt number versus Rayleigh number, viscous terms in the momentum equations approximated by a Darcy type relation, adiabatic sidewalls, ——— Darcy approximation, --- viscous terms included.